**ALMA MATER STUDIORUM**
**UNIVERSITÀ DI BOLOGNA**

SECONDA FACOLTÀ DI INGEGNERIA
SEDE DI FORLÌ

CORSO DI LAUREA MAGISTRALE IN
INGEGNERIA AEROSPAZIALE
CLASSE LM-20

TESI DI LAUREA IN TOLLERANZA AL DANNO
DI STRUTTURE AERONAUTICHE LM

# "INFLUENCE OF MICROSTRUCTURE VARIABILITY ON SHORT CRACK GROWTH BEHAVIOR"

**RELATORE:**
Prof. Ing. Enrico TROIANI

**CANDIDATO:**
Andrea ROVINELLI

**CORRELATORE:**
Prof. Michael D. SANGID
PURDUE UNIVERSITY

ANNO ACCADEMICO 2012/2013
SESSIONE I

*Ai miei genitori,*

*a Francesca,*

*a Cristina,*

*e a tutte le persone che*

*mi hanno aiutato a*

*raggiungere questo*

*importante traguardo*

*To my parents,*

*to Francesca,*

*to Cristina,*

*and to all the people*

*who helped me*

*to achieve this*

*important goal*

**Ringraziamenti**

Vorrei ringraziare i *miei genitori*, *Daniele* e *Rita*, per avermi insegnato a non mollare mai davanti alle difficoltà e ad inseguire i miei sogni, mia *sorella Francesca* per avermi insegnato la caparbietà necessaria a raggiungere traguardi difficili, alla mia *fidanzata Cristina* per avermi spronato e sopportato durante questi anni e avermi concesso la tranquillità necessaria durante questi 9 mesi trascorsi negli *Stati Uniti d'America* a redigere questa tesi.

Un ringraziamento speciale va al mio correlatore, il *Prof Michael D. Sangid* che mi ha accolto nel suo laboratorio alla *Purdue University*, che mi ha guidato durante questa attività di ricerca insegnandomi la disciplina della "ricerca scientifica", e che mi ha dato la possibilità di continuare il cammino di ricercatore attraverso un dottorato di ricerca.

Inoltre, vorrei ringraziare il mio relatore, il *Prof. Enrico Troiani* per avermi guidato nella scelta del progetto di tesi e per essere stato una guida insostituibile durante questi anni di corso, sia a livello professionale che umano.

Un altro ringraziamento va ai miei colleghi di studio *Ing. Andrea Rizzo* e *Ing. Valentina Cantarini* con i quali ho condiviso lo studio di molte materie e la fantastica esperienza di partecipare ad una competizione internazionale per studenti, *Aerodays-2011*, che ci ha portato a presentare il nostro progetto a *Madrid*. A loro auguro una brillante carriera.

**Acknowledgements**

I would like to thank *my parents*, *Daniele* e *Rita*, for teaching me to never give up when faced with difficulties and to pursue my dreams, my *sister Francesca* for teaching me the stubbornness needed to achieve difficult goals, my *fianceé Cristina* for having encouraged me, for her patience during these years and for giving me the necessary peace during these 9 months spent in the *United States of America* to prepare this thesis.

A special thanks goes to my co-supervisor, *Prof Michael D. Sangid*, who has welcomed me into his laboratory at *Purdue University*, who has guided me during this research teaching me the discipline of " scientific research", and who has given me the opportunity to continue my career as a researcher through a PhD.

Also, I would like to thank my supervisor, *Prof. Enrico Troiani* for guiding me in choosing this thesis project and for being an invaluable guide during these years, both professionally and personally.

Another thanks goes to my fellow students *Eng. Andrea Rizzo* and *Eng. Valentina Cantarini* with whom I shared the study of many classes and the fantastic experience of participating in an international competition for students, *Aerodays-2011*, which led us to present our project in *Madrid*. I wish them a successful career.

**Sommario**

La vita a fatica dei materiali metallici è predetta utilizzando analisi di regressione su grandi quantità di dati sperimentali, tramite l'utilizzo di modelli matematici basati sulla risposta macroscopica dei materiali. Inoltre, è ben nota una grande incertezza del tasso di crescita nel regime di "Short Crack Growth (SCG)" per materiali policristallini, in cui l'evoluzione e la distribuzione della plasticità locale è fortemente influenzata dalle caratteristiche della microstruttura. Lo scopo di questa tesi è (a) di identificare la relazione tra la "crack driving-force" e le caratteristiche della microstruttura presente in prossimità della "crack-tip" e (b) definire la correlazione tra l'incertezza osservata nel tasso di crescita nel regime di "Short Crack Growth" e la variabilità nella microstruttura locale. Per raggiungere questi traguardi, si è utilizzata la formulazione spettrale (Fast Fourier Transform) del problema elasto visco-plastico del modello di "Crystal Plasticity" (CP-EVP-FFT), poiché la possibilità di tener conto contemporaneamente del regime elastico e plastico è fondamentale nei problemi di fatica. Infatti, il fenomeno della crescita della cricca è governato dall'irreversibilità dello slittamento dei piani cristallini (slip irreversibilities), generato durante l'applicazione ciclica del carico, che inizia a verificarsi durante la transizione elasto-plastica locale del materiale. Per investigare gli effetti della variabilità della microstruttura sul tasso di crescita della cricca nel regime di SCG, differenti realizzazioni della microstruttura sono state costruite, in cui cricche di differenti lunghezze sono state inserite, al fine di mimare l'avanzamento della cricca nei materiali ingegneristici. Dai risultati di queste simulazioni le grandezze caratteristiche delle diverse scale di lunghezza vengono analizzate: (i) il campo degli degli sforzi di Von Mises , (ii) la proiezione del tensore degli sforzi/allungamenti sui relativi piani cristallini (resolved shear-stress/strain) e (iii) l'accumulo dello slittamento e le irreversibilità dello stesso. Attraverso l'utilizzo dei "Fatigue Indicator Parameters" l'incertezza del tasso di

crescita nel regime di SCG viene correlata alla variabilità delle caratteristiche nella microstruttura; i risultati dimostrano come questa relazione tra variabilità nella microstruttura e incertezza nel comportamento a fatica sia critica per la corretta stima della vita dei componenti ingegneristici.

**Abstract**

Fatigue life in metals is predicted utilizing regression analysis of large sets of experimental data, thus representing the material's macroscopic response. Furthermore, a high variability in the short crack growth (SCG) rate has been observed in polycrystalline materials, in which the evolution and distribution of local plasticity is strongly influenced by the microstructure features. The present work serves to (a) identify the relationship between the crack driving force based on the local microstructure in the proximity of the crack-tip and (b) defines the correlation between scatter observed in the SCG rates to variability in the microstructure. A crystal plasticity model based on the fast Fourier transform formulation of the elasto-viscoplastic problem (CP-EVP-FFT) is used, since the ability to account for the both elastic and plastic regime is critical in fatigue. Fatigue is governed by slip irreversibility, resulting in crack growth, which starts to occur during local elasto-plastic transition. To investigate the effects of microstructure variability on the SCG rate, sets of different microstructure realizations are constructed, in which cracks of different length are introduced to mimic quasi-static SCG in engineering alloys. From these results, the behavior of the characteristic variables of different length scale are analyzed: (i) Von Mises stress fields (ii) resolved shear stress/strain in the pertinent slip systems, and (iii) slip accumulation/irreversibilities. Through fatigue indicator parameters (FIP), scatter within the SCG rates is related to variability in the microstructural features; the results demonstrate that this relationship between microstructure variability and uncertainty in fatigue behavior is critical for accurate fatigue life prediction.

# Contents

# List of Figures

# List of Tables

# Chapter 1

# Introduction

## 1.1 Plasticity

From a macroscopic point of view, plasticity occurs when, after loading a material over its yielding stress/strain, $\sigma_y/\varepsilon_y$, it will not recover its initial shape, see Figure 1.1(a). Looking at the stress/strain curve, if we unload the material after the stress has reached the value of $\sigma_l$, there will be a residual plastic strain that we define as $\varepsilon_{pl}$. Also we can note that the yielding stress $\sigma_y$ is the end of the proportional relationship between stress and strain. Furthermore, after that yielding has occurred, the relationship between stress and strain is not unique: at each value of stress/strain corresponds to more than 1 value of strain/stress.

The concepts that we have just mentioned raise different tasks:

- when the material is yielding, discover how it changes shape
- find a convenient quantity that can take into account the loading history and the change in shape of the material
- understand what is happening inside the material and why the relationship between stress and strain is not proportional

These tasks are obviously related but let's start from the latter. The first

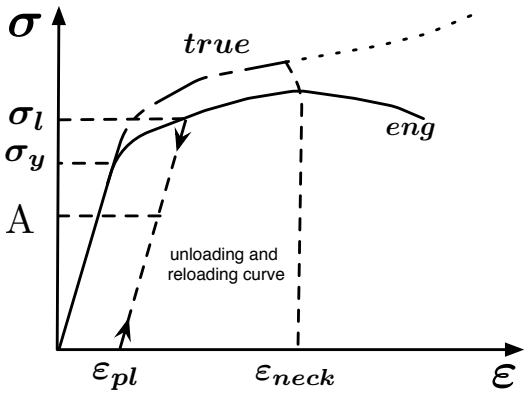


(a) typical stress vs strain diagram for a ductile material depicting Engineering and True plots

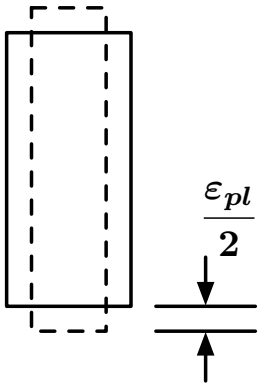


(b) residual strain after unloading a yielded specimen (solid line before yielding, dotted line after unloading)

**Figure 1.1**

thing that we need to know is when does plasticity first occurs, which can be quantified utilizing the *Yielding criteria*. Experiments has found that plastic deformation are not caused by hydrostatic stress, that can be stated mathematically as $\sigma_{11} = \sigma_{22} = \sigma_{33}$ in principal stress axes (from now on we always will be in principal stress axes), let's define the deviatoric stress tensor as

$$\sigma' = \sigma - \frac{1}{3} trace(\sigma) I \tag{1.1}$$

where $I$ is the identity matrix. The most common test utilized to find the yielding properties of a material is the uniaxial tensile test which has just one stress value for yielding, $\sigma_y$, so we need to define an equivalent stress $\sigma_{eq}$ as a function of all the components of the deviatoric stress tensor $\sigma_{eq} = \sigma_{eq}(\sigma')$. This is also useful from a computational point of view, in fact the most important engineering equivalent stress is the *Von Mises equivalent stress*: this will reduce the problem from 6 to 1 dimension. The more general formulation

in non principal stress axes is:

$$\sigma_{eq,VM} = \sqrt{\frac{1}{2}\left((\sigma_{11}-\sigma_{22})^2 + (\sigma_{11}-\sigma_{33})^2 + (\sigma_{22}-\sigma_{33})^2 + 3\left(\sigma_{32}^2 + \sigma_{31}^2 + \sigma_{12}^2\right)\right)} \tag{1.2}$$

Now we can define the so called *Yielding Function* as

$$f(\sigma_{eq,VM}, \sigma_y) = \sigma_{eq,VM} - \sigma_y \tag{1.3}$$

Naturally we will not have yielding until $f(\sigma_{eq,VM}, \sigma_y) < 0$.

If we depict the *Yielding Function* in the stress space we will find the *Yield Surface* that, using the Von Mises Criterion, has a cylindrical shape with the center on the hydrostatic stress point (we can also use other yield criterion like the Tresca one).

Now that we know when the first plastic deformation will occur, we can look at what happens after this point. During a tensile test, until a certain value of strain that we will define as $\varepsilon_{neck}$, the volume of the specimen remains constant: this means that no voids are created. We can easily state a constant volume equation: $A_0 * l_0 = A_f * l_f$, where the subscript 0 refers to the initial values and $f$ refers to final values. Deriving this equation, remembering the definition of engineering strain ($\varepsilon_{eng} = \frac{l_f - l_0}{l_0}$), and applying the integral between $l_0$ and $l_f$ of $d\varepsilon_{eng}$ allow us to define a new type of strain known as the true strain:

$$\varepsilon_{true} = \int_{l_0}^{l_f} \frac{dl}{l} = \ln(1 + \varepsilon_{eng}) \tag{1.4}$$

After defining a true strain we can define a true stress also: $\sigma_{true} = \frac{F}{A(l)}$. Using this equation together with the constant volume hypothesis, the definition of engineering strain and stress we find:

$$\sigma_{true} = \frac{F}{A(l)} = \frac{F l_i}{S_0 l_0} = \sigma_{eng}(1 + \varepsilon_{eng}) \tag{1.5}$$

We should note that all this treatment is valid only if the cross section of the

specimen is constant along his whole length, and until $\varepsilon_{eng} \leq \varepsilon_{neck}$, in any other case it is required carefully account for the geometry.

Lets now introduce the *Flow Rules*, that is the description of how the material plastically deforms. Even if, whenever a plastic deformation occurs the relation between stress and strain is not unique, we can still calculate how much stress $\sigma$ we need to obtain an infinitesimal increment of plastic strain $d\varepsilon_{pl}(\sigma)$ because the yield criteria (Von Mises or Tresca) must be fulfilled. For convenience of measure, we now define the plastic strain rate as

$$d\dot{\varepsilon}_{pl} = \frac{d\varepsilon_{pl}(\sigma)}{dt} = \dot{\lambda}\sigma \tag{1.6}$$

where $\dot{\lambda}$ is a proportional factor, that besides its dependencies from the material, adjust itself at any given strain rate to ensure that the deviatoric stress cannot leave the yielding surface.[1]

By looking closer at the stress and strain diagram, we can note that after yielding has occurred we still need to increase the stress to increase the strain, this phenomena is know as *Strain Hardening* and is driven by the *Hardening Law* that we will discuss later. The stress state must always lay inside the yielding surface, or at least at its boundary. This suggest that the Yielding Surface must change during plastic deformation, moreover that during plastic deformation the yield criterion must be dynamic, which can be mathematically expressed by introducing some additional terms. We introduce now a new Yielding Function:

$$g = g(\sigma, \varepsilon_{pl}, k_l) = 0 \tag{1.7}$$

where $\varepsilon_{pl}$ is the current plastic deformation, and $k_l$ is a set of hardening parameters that may depends on deformation history, strain rate and temperature. To take hardening into account we need to define a quantity that must increase at each plastic deformation and that remembers all plastic deformation:

[1] **Note:** to derive the Equation 1.6 we must use the Drucker's postulate that states that during plastic deformations we need to maximize the dissipated power.

it is the so called *equivalent plastic strain* that can be found integrating the *equivalent plastic strain rate* defined as:

$$\dot{\varepsilon}^{pl}_{eq} = \sqrt{\frac{2}{9}\left[(\dot{\varepsilon}^{pl}_{11} - \dot{\varepsilon}^{pl}_{22})^2 + (\dot{\varepsilon}^{pl}_{11} - \dot{\varepsilon}^{pl}_{33})^2 + (\dot{\varepsilon}^{pl}_{22} - \dot{\varepsilon}^{pl}_{33})^2\right]} \tag{1.8}$$

As we can see is very similar to the Von Mises equivalent stress in principal stress axes, also the parameter $k_l$ is a function of the equivalent plastic strain $k_l = k_l(\varepsilon^{pl}_{eq})$. We can also observe that equation (1.7) = (1.3), if $\varepsilon_{pl} = 0$.

As we said before we need an *Hardening Law* to take in to account the *Strain Hardening* phenomena. We can define the *Flow Stress*, $\dot{\sigma}_F$, that is the instantaneous value of stress required to continue deforming the material, or can also be seen the stress required to sustain plastic deformation at a particular strain. The most simple Hardening Rule that we can think is linear and has the form

$$\begin{cases} \dot{\sigma}_F = & H\dot{\varepsilon}^{pl}_{eq} \\ \dot{\sigma}_F(t_0) = & \sigma_y \end{cases} \tag{1.9}$$

where $H$ is the Hardening Parameter.

## 1.2 Slips System

We can now change our perspective and look what's happening at smaller scale: the microscopic level. As we are mainly interested in metals, we should remember that this material, at solid phase, organize themselves in an ordered configuration called crystal lattice. It's well know that nature itself always try to minimize the potential energy and this is not an exception: the distance between neighbors atoms depends on the potential energy of their attractive and repulsive forces. Because of this and the fact that different materials has different electronic configuration, which implies a number of different nearest neighbors, and different radius we expect to have different lattice type. All the possible configuration are included in the Bravais Lattice show in Figure 1.2 and all the geometrical characteristic are in Table 1.1. We should note that this kind of configurations have the characteristic to fill the material without leaving void and are called *Unit Cells* (we can see them as the "building blocks" of the lattice). Each of these unit cell is characterized by 6 parameters: 3 lengths and 3 angles (see Figure 1.3).

Now that we know how the atoms are arranged we need a conventional way to identify directions and planes and the most conventional way is to utilize *Miller Indexes*. The peculiarity of these Indexes is that they are always composed by integer number and can illustrate

- directions i.e. $[111]$ or $[\bar{1}00]$
- planes i.e. $(111)$ or $(1\bar{1}1)$
- set of equivalent directions i.e. $\langle 111 \rangle$ or $\langle \bar{1}00 \rangle$
- set of equivalent planes i.e. $\{111\}$ or $\{\bar{1}00\}$

Note that the bar over a number identify a negative index and different kind of parentheses have different meaning, also they represent the direction cosine for directions and the cosine direction of the normal of the plane for the planes (in

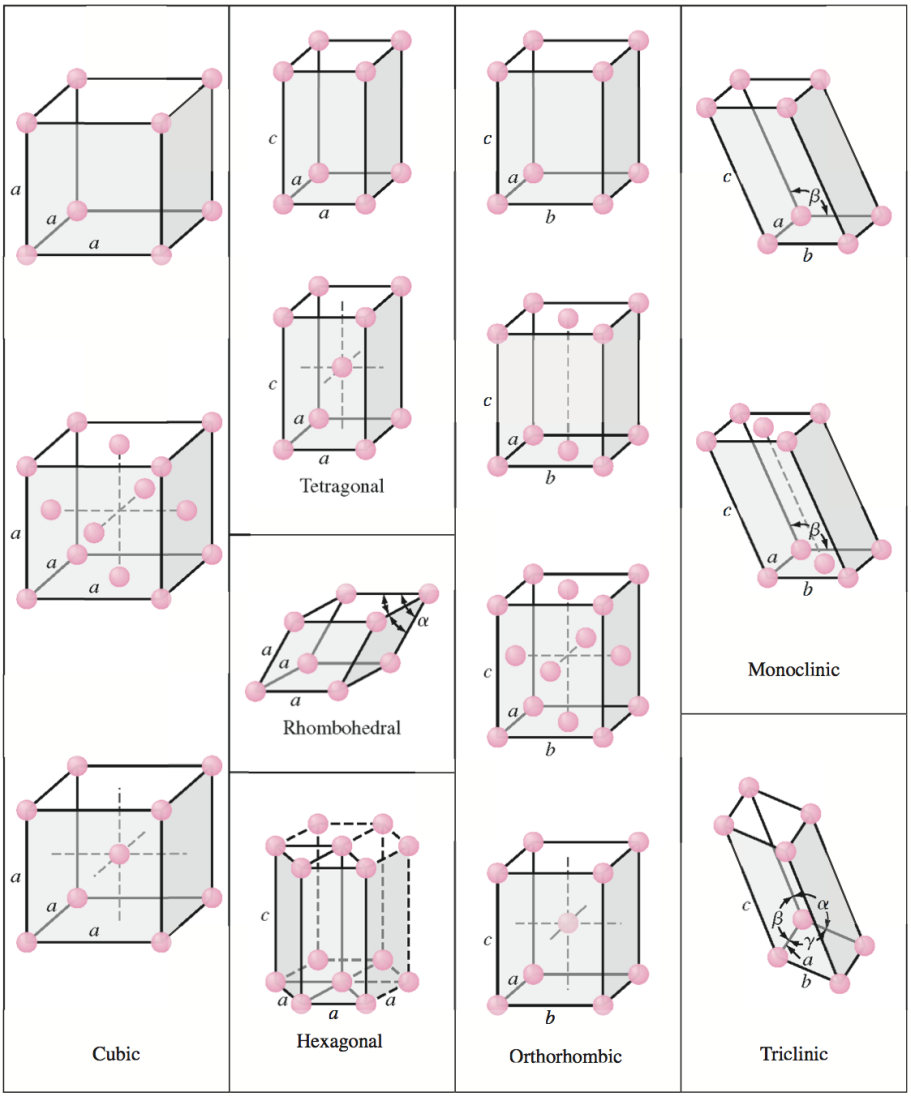


**Figure 1.2:** All 14 Bravais lattice types (image from Smith and Hashemi [56])

cubic crystal) both using integer number, so that their modules can differ from 1 see Figure 1.4. It's important to note that due to the fact that the crystal lattice is well organize and that is build from many unit cells, all with same shape, it has many equivalent directions and planes for example in a Simple-Cubic lattice if we write $\langle 001 \rangle$ we are meaning $[001]$,$[00\bar{1}]$,$[010]$,$[0\bar{1}0]$,$[100]$,$[\bar{1}00]$, in fact for an observers positioned on one atom all of this direction are indistinguishable. The same reasoning can be applied to planes: write $\{111\}$ means $(111), (11\bar{1}), (1\bar{1}1), (1\bar{1}\bar{1}), (\bar{1}11), (\bar{1}1\bar{1}), (\bar{1}\bar{1}1), (\bar{1}\bar{1}\bar{1})$ If we think of atoms as rigid

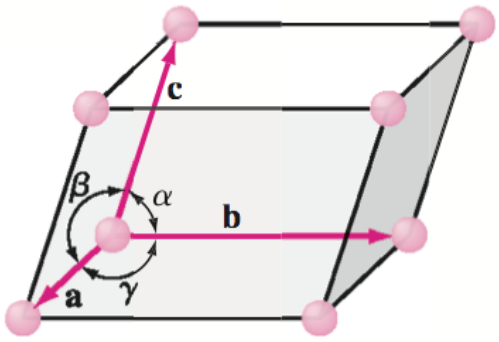


**Figure 1.3:** meaning of the 6 constants of a unit cell (image from Smith and Hashemi [56])

| Crystal system | Axial lengths and interaxial angles | Space lattice |
|---|---|---|
| Cubic | Three equal axes at right angles<br>$a = b = c, \alpha = \beta = \gamma = 90°$ | Simple cubic<br>Body-centered cubic<br>Face-centered cubic |
| Tetragonal | Three axes at right angles, two equal<br>$a = b \neq c, \alpha = \beta = \gamma = 90°$ | Simple tetragonal<br>Body-centered tetragonal |
| Orthorhombic | Three unequal axes at right angles<br>$a \neq b \neq c, \alpha = \beta = \gamma = 90°$ | Simple orthorhombic<br>Body-centered orthorhombic<br>Base-centered orthorhombic<br>Face-centered orthorhombic |
| Rhombohedral | Three equal axes, equally inclined<br>$a = b = c, \alpha = \beta = \gamma \neq 90°$ | Simple rhombohedral |
| Hexagonal | Two equal axes at 120°, third axis at right angles<br>$a = b \neq c, \alpha = \beta = 90°, \gamma = 120°$ | Simple hexagonal |
| Monoclinic | Three unequal axes, one pair not at right angles<br>$a \neq b \neq c, \alpha = \gamma = 90° \neq \beta$ | Simple monoclinic<br>Base-centered monoclinic |
| Triclinic | Three unequal axes, unequally inclined and none at right angles<br>$a \neq b \neq c, \alpha \neq \beta \neq \gamma \neq 90°$ | Simple triclinic |

**Table 1.1:** Characteristic of all the different type of unit cells (table from Smith and Hashemi [56])

spheres arranged in a crystal lattice, due to the fact that different directions have different distance between atoms i.e.$\langle 001 \rangle$ and $\langle 011 \rangle$ (the same is valid for planes) we will find preferred slipping directions on preferred slipping planes. The slip will occur on the *closest pack direction* (with minimum distance between atoms) on the *closest packed plane* (with maximum distance between

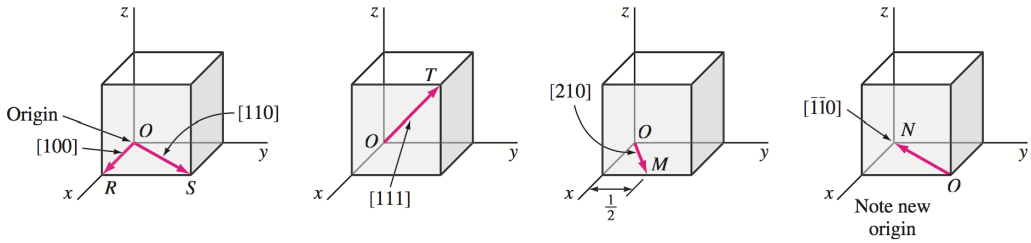


(a) Use of Miller Indexes for planes (image from Smith and Hashemi [56])

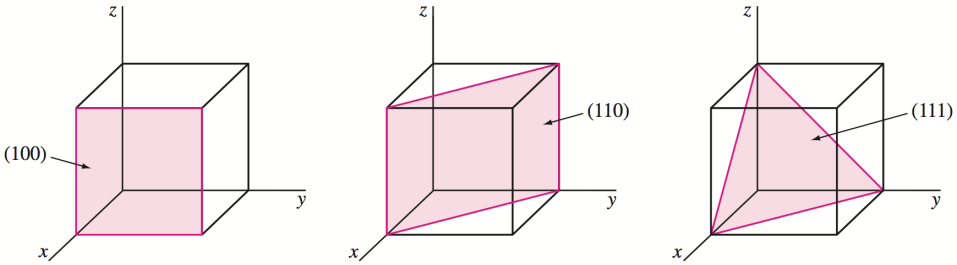


(b) Use of Miller Indexes for planes (image from Smith and Hashemi [56])

**Figure 1.4**

parallel planes). A combination of Slip Plane and Slip Direction is called *Slip System* and each type of unit cell has its own Slips Systems (i.e. a Face Centered Cubic crystal has 12 Slips Systems defined as $\langle 110 \rangle$-$\{111\}$)

If we consider shearing a single crystal as an example, it can be deformed plastically by sliding whole layers of atoms against each other (as we said in the previous section plastic deformation are permanent, thus we realize that the atomic configuration changes). The ideal stress required for this process can be estimated and is of the order of one fifth of the shear modulus of the crystal. The yield strength predicted this way for metallic single crystals is thus between 1 $GPa$ and 25 $GPa$ (see rosler) that is orders of magnitude greater than the value measured for pure single crystal material. The explanation for this big difference between theoretical and measured value, is attributed to crystal defects of which *dislocations* are the most important.

Dislocations are one dimensional (line-shaped) defects of the crystal lattice and it's structure can be visualized imagining that an additional half-plane of

atoms is added/removed to/from the crystal. In the vicinity of the line where this half plane ends, the crystal is distorted, further away from it, it still is perfect. Dislocations are characterized by 2 parameters *Burgers Vector* and *Dislocation Line*. The former that can be determined in the following way: We draw a so-called Burgers circuit around the dislocation line that takes the same amount of steps from one atom to the next in each direction as visualized in Figure 1.5 We can idealize 2 extreme types of dislocation: *Edge Dislocations* and *Screw Dislocations*, but in the real world the dislocation line can be curved thus we can idealize the curved dislocation as a linear combination of both. It

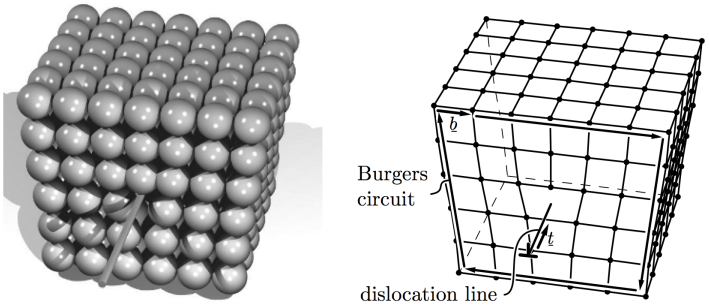


(a) Edge dislocation

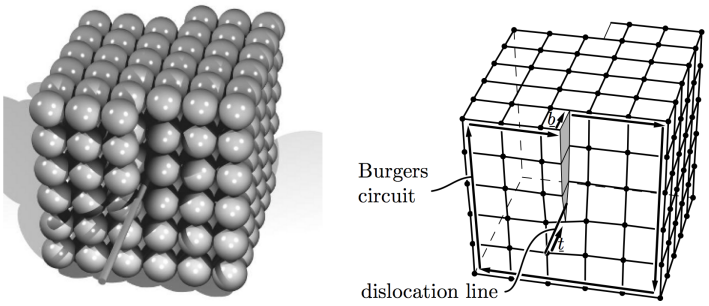


(b) Screw dislocation

**Figure 1.5:** Edge and Screw dislocations schematic (image from Rösler et al. [49])

should be noted that dislocation lines are always either closed or end at the surface of the crystal, but they can never end within the crystal. The vacancy that the dislocation introduce in the lattice interact with the potential energy of atoms, causing a stress field that will act as a catalyst for the slipping system and will make the dislocation move in many different way and interact between themselves, annihilating and piling up.

## 1.3 Crystal Orientation

As can be inferred from the previous section, the projection of the stress on a particular slip system depends on relative orientation between the unit cell and the stress applied to it. For this and other reasons, we need a mathematical formulation of the orientation of the crystal.

The easiest way to identify a rotated object in the space is through *Euler's Angle* defined as $\psi, \theta, \phi$ [2]. Let's define the Euler's Angle as the angle of rotation needed to rotate a vector from the sample reference system to the crystal reference system and matrix $R_{s\to c} = R_{s\to c}(\psi, \theta, \phi)$ as the matrix that will perform this rotation (due to the definition of rotation matrix if we want to go from crystal to sample we will use $R^T_{s\to c} = R_{c\to s}$). This will allow us to rotate any vector from the sample reference system (that we will call $\bar{v}_s$), where we know exactly the coordinates of planes and directions expressed with Miller Indexes, to the crystal reference system or vice versa. So we can define the rotated vector $\bar{v}_c$ as:

$$\bar{v}_c = R_{s\to c}\bar{v}_s \tag{1.10}$$

There are two common way to illustrate the characteristic of a polycrystalline material in a chart. This is done with two different type of *Stereographic Projection* (see Figure 1.6 for the scheme of the projection):

- *Pole Figure* (PF)

    1. take the sets of normals to plane of interest i.e. $\bar{n}_s = \langle 111 \rangle$ and normalize it
    2. apply the rotation from sample to crystal reference $\bar{n}_c = R_{s\to c}\bar{n}_s$
    3. convert $\bar{n}_s$ from cartesian to spherical coordinate ($\rho = 1$, $\theta = \cos^{-1}(n_{c,z})$, $phi = \tan^{-1}(\frac{n_{c,y}}{n_{c,x}})$)

[2] In the crystallographic theory there are many possible angle's convention Bunge, Kocks, Canova, Roe. They differ not only for the convention of the signs of angles but also for the axes on which the second rotation has been performed.

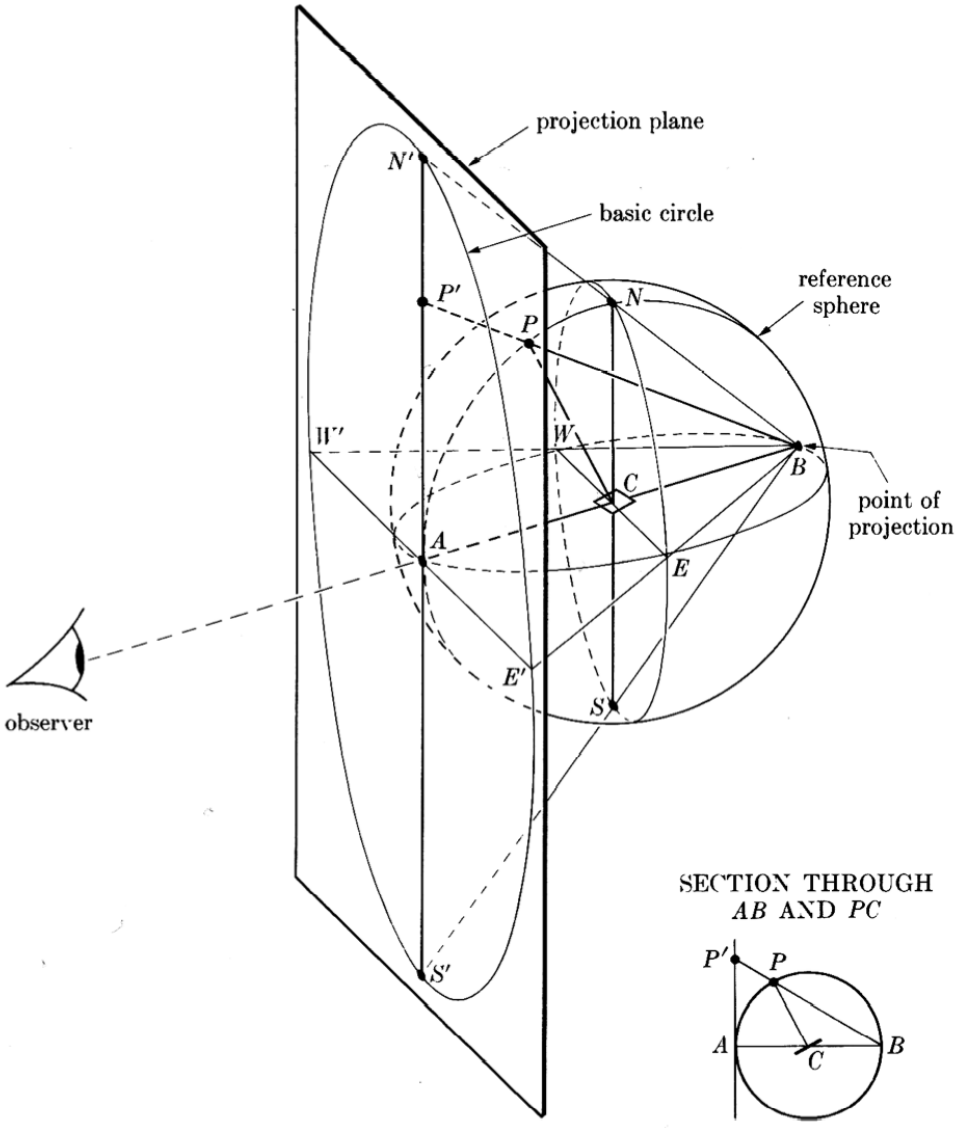


**Figure 1.6:** Scheme of a generic stereographic projection

4. project on the standard plane (001): $x = \tan(\frac{\theta}{2})\cos(\phi)$, $y = \tan(\frac{\theta}{2})\sin(\phi)$ and discard

- *Inverse Pole Figure* (IPF)

1. take the direction of interest: i.e. [001]
2. apply the rotation from crystal to sample reference $\bar{n}_s = R_{c\to s}\bar{n}_c$
3. steps 3 and 4 are the same of the pole figure

These charts are both utilized to characterized important geometries features for example we can identify crystal with orientation more prone to slipping than others, or filtering some particular orientation range we can identify the percentage of specific texture component like Goss, S, Copper, Cubic. Another particular features that we should list is that with standard IPF we need 3 charts to have complete information about an orientation while with the standard PF, one chart is enough. Also these charts are subjected to the same number of symmetries of the unit cell type that they are representing, and the fundamental zone that we have to look to have complete information is $\frac{1}{\#symmetries}$ (Rollett [48]). **The code for both Pole and Inverse Pole figure has been implemented, tested and validated**: we can see the IPF and he PF respectively in Figure 1.7 and in Figure 1.8. We should note the 24 fold-symmetry of the IPF due to the Cubic Crystal features and how each one of the stereographic triangles is equivalent to another. We note that only the poles that are on the north are plotted, so instead of having 8 projections we have only 4 of them. The PF is useful to understand the dependence of the Resolved Shear Stress (see Section 1.4 and Equation 1.15) from the load direction see Figure 1.9

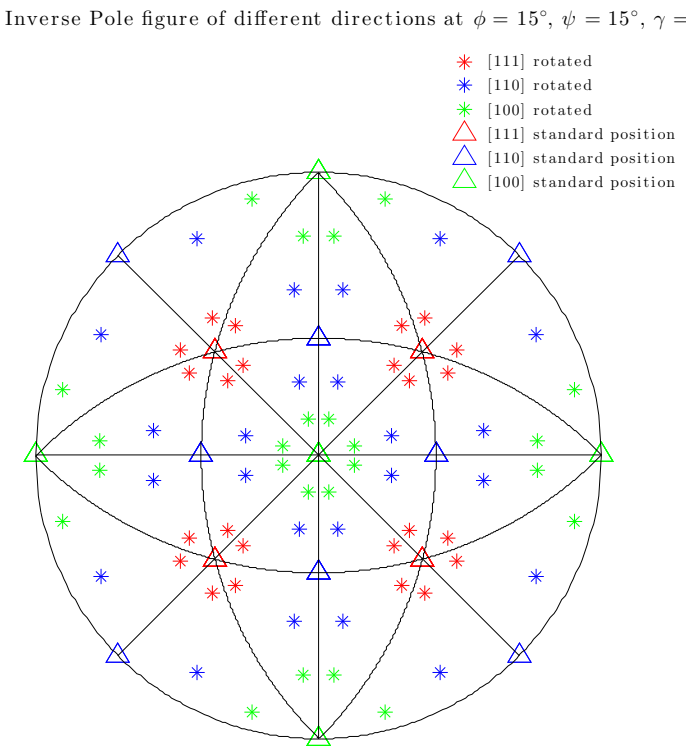


**Figure 1.7:** Inverse Pole Figure

## 1.4 Resolved Shear Stress

Lets think of a single crystal specimen during a tensile test casually oriented in which we know the rotation matrix $R_{s\to c}$, and it's cross section surface $A_0$, we are able to calculate the projection of the stress on each slip system. In the Figure 1.10 we define $\bar{n}$ and $\bar{m}$ as respectively the normal to the slipping plane and as the slip direction (both using Miller Indexes), $F$ as the applied load, $\theta$ as the angle between $F$ and $\bar{n}$, $\lambda$ as the angle between $F$ and $\bar{m}$ and $A$ as the surface of the specimen. The first thing that we need to do is to normalize the

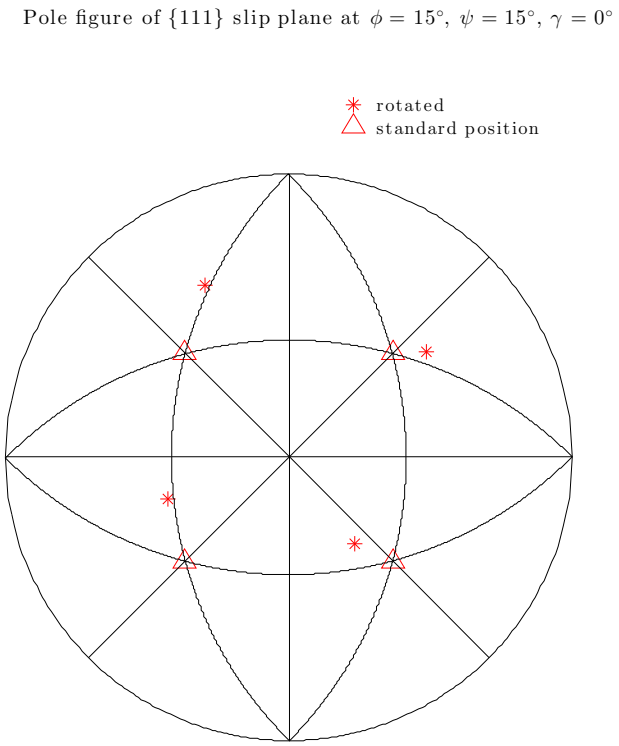


**Figure 1.8:** Pole Figure

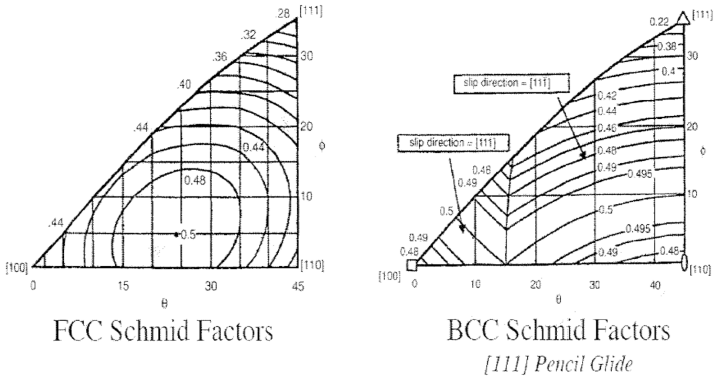


**Figure 1.9:** Schmid's Factor dependence on load orientation

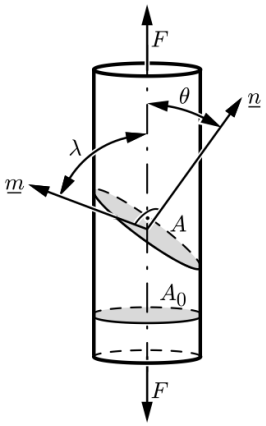


**Figure 1.10:** Tensile test with plane normal and direction highlighted (image from Rösler et al. [49])

3 vectors that we have defined

$$\hat{F} = \frac{F}{\|F\|} \qquad \hat{n} = \frac{n}{\|n\|} \qquad \hat{m} = \frac{m}{\|m\|} \tag{1.11}$$

Now we can rotate the crystal plane and direction using Equation 1.10

$$\hat{n}_c = R_{s\to c}\hat{n} \qquad \hat{m}_c = R_{s\to c}\hat{m} \tag{1.12}$$

and find $\theta$ and $\lambda$ simply by doing the dot product of these angles (defined in Figure 1.10) with $F$

$$\theta = \hat{F} \cdot \hat{n}_c \qquad \lambda = \hat{F} \cdot \hat{m}_c \tag{1.13}$$

now the area of the inclined slip plane and the projection of the force on the slip direction are respectively

$$A = \frac{A_0}{\cos(\theta)} \qquad F_m = F\cos(\lambda) \tag{1.14}$$

If we now relate both forces to the area they are acting upon and defining the shear stress over a slip system as $\tau^{rss} = F_m/A$ and $\sigma = F/A_0$ we can write the

final equation for the resolved shear stress for this easy case as

$$\tau^{rss} = \sigma \cos(\lambda) \cos(\theta) \tag{1.15}$$

where the product $\cos(\lambda)\cos(\theta)$ is called *Schmid's Factor*. If we now want to take into account a generic stress state we need to use a tensorial notation. The physical meaning of the equation remains the same: we are projection all the traction vector of the stress tensor on each slip system in order to find the resolved shear stress:

$$\hat{\tau}^{rss} = \hat{m}_i \sigma_{i,j} \hat{n}_j = \frac{1}{2}\sigma : (\hat{n} \otimes \hat{m} + \hat{n} \otimes \hat{m}) \tag{1.16}$$

where ":" is the *double dot product*, whom results is a scalar, and "$\otimes$" is the *Diadic product*, that create a $2^{nd}$ order tensor multiplying two $1^{st}$ order tensor (vector). Note that $\hat{n}$ and $\hat{m}$ are unit vectors and, if necessary, have to be rotated in the the stress reference system utilizing the equation. Note that the product

$$\frac{1}{2}(\hat{n} \otimes \hat{m} + \hat{n} \otimes \hat{m}) \tag{1.17}$$

is usually called the *Schimd's Tensor*.

## 1.5 CP-EVP-FFT code and model

We are going to introduce the *CP-EVP-FFT code* (where CP stands for Crystal Plasticity, EVP for Elasto-ViscoPlastic and FFT for Fast Fourier Transform) that we will use to investigate the material behaviour at microscopic scale. The elasto-viscoplastic fast Fourier transform-based model (CP-EVP-FFT) developed by Lebensohn et al. [27], is an extension of classical crystal plasticity theory (Asaro [5]). The FFT framework represents an efficient modeling technique originally developed by Moulinec and Suquet [34, 35] for both linear elastic and nonlinear elasto-plastic composites, and subsequently extended to viscoplastic composites byMichel et al. [30, 31]. The CP-EVP-FFT model used in this study is the most general formulation of two previous models for polycrystalline deformation in the elastic regime (Brenner et al. [9]) and the rigid viscoplastic regime (Lebensohn [26], Lebensohn et al. [24, 25], Lee et al. [28]). Nowadays, very large, high-fidelity 3D images of polycrystalline aggregate microstructures are available and can be obtained with different reconstruction techniques, such as iterative electron backscatter diffraction (EBSD) and synchrotron-based high-energy x-ray diffraction microscopy (HEDM); the results of these scans are crystallographic features, such as grain orientation and phases, arranged in a regular spaced grid of points with subgrain/submicron resolution. The advantage of CP-EVP-FFT as an image-based technique is the possibility to directly utilize the crystallographic features as an input into the modeling techniques without the needing to homogenize the orientation within each grain as required by FEM methods. As a consequence, larger models can be ran with the CP-EVP-FFT method, due to its computational efficiency. In this methodology, a macroscopic strain or strain-rate, respectively $E_{ij}$ and $E'_{ij}$, is imposed on the unit cell and the response to this mechanical boundary condition, in terms of stress and strain-rate fields, is determined. The CP-EVP-FFT algorithm computes a compatible strain-rate field, associated with a kinematically admissible velocity field that

minimizes the average work rate and satisfies at every point the constitutive differential relation governing the micromechanical problem with an equilibrated stress field. As we discussed in the previous sections of this report, many constitutive parameter of the material must be taken into account to describe the evolution of stress and strain microfields, which extreme values dictate the macroscopic behaviour:

- the unit cell type and its own slip systems
- the critical resolved shear stress
- the hardening law: type and parameters
- the stiffness/compliance matrix associated with the unit cell (i.e. materials with FCC unit cell haven't an isotropic behavior )
- the strain rate sensitivity
- self and latent hardening coefficient
- and crystal plasticity model

With all these information for each points of the grid the CP-EVP-FFT formulation can describe the elasto-viscoplastic response to an external forced strain or strain-rate of a *periodic microstructure* (this limitation is due to the FFT method) providing an exact solution. Let's see how all this parameter and laws are used together to implement this code.

## 1.6 Elasto Visco Plastic formulation

Utilizing the rigid-viscoplastic approximation of crystal plasticity (Lebensohn [26]), that implies negligible elastic strain compared with the plastic one, the relation between visco-plastic strain-rate $\dot{\boldsymbol{\varepsilon}}^p(\boldsymbol{x})$ and $\boldsymbol{\sigma}(\boldsymbol{x})$ at a single crystal

material point $\boldsymbol{x}$ through a sum over $N$ active slip systems of the form:

$$\begin{aligned}\dot{\boldsymbol{\varepsilon}}^{pl}(\boldsymbol{x}) &= \sum_{\alpha=1}^{N} \boldsymbol{M}^{\alpha}(\boldsymbol{x})\dot{\gamma}^{s}(\boldsymbol{x}) \\ &= \dot{\gamma}_0 \sum_{\alpha=1}^{N} \boldsymbol{M}^{\alpha}(\boldsymbol{x}) \left( \frac{|\boldsymbol{M}^{\alpha}(\boldsymbol{x}) : \boldsymbol{\sigma}(\boldsymbol{x})|}{\tau_0^{\alpha}(\boldsymbol{x})} \right)^{n} \operatorname{sgn}(\boldsymbol{M}^{\alpha}(\boldsymbol{x}) : \boldsymbol{\sigma}(\boldsymbol{x}))\end{aligned} \tag{1.18}$$

where $\dot{\gamma}(\boldsymbol{x})^{\alpha}$ is the shear rate, $\tau_0^{\alpha}(\boldsymbol{x})$ is the CRSS (critical value of stress needed to activate the slip system) and $\boldsymbol{M}^{\alpha}$ is the Schmid Tensor (see Equation 1.17) all associated to the slip system $s$ at the material point $\boldsymbol{x}$, while $\gamma_0$ is a normalizing parameter needed to set the reference value of the strain rate at which the CRSS was calculated, and n is the stress exponent, or the inverse of the rate sensitivity exponent which takes into account the dependence of the CRSS from the strain rate. We should note that this kind of formulation use a phenomenological approach and doesn't take into account the physics that is happening at atomistic level or, in other words, dislocations mechanics; from the other hand we should note that all the parameter required as input in this code, except the texture orientation, can be found from simple, well established and relatively inexpensive tests, without the needing to use computationally expensive molecular dynamics simulations.

If we want to take into account the elastic behaviour, that is important to evaluate both the change in spacing in the lattice, or the development of the stress concentration field, that leads to damage during cyclic deformation, we need to remember that we can decompose the total strain as follow:

$$\boldsymbol{\varepsilon}_{tot} = \boldsymbol{\varepsilon}_{el} + \boldsymbol{\varepsilon}_{pl} = \boldsymbol{S}\boldsymbol{\sigma} + \boldsymbol{\varepsilon}_{pl} \tag{1.19}$$

where $\boldsymbol{S}$ is the compliance tensor. After this, using a simple implicit Euler

time discretization, we can easily write

$$\boldsymbol{\sigma}^{t+\Delta t}(\boldsymbol{x}) = \boldsymbol{C} : \boldsymbol{\varepsilon}^{e,t+\Delta t}(\boldsymbol{x}) \tag{1.20}$$
$$= \boldsymbol{C} : [\boldsymbol{\varepsilon}^{t+\Delta t}(\boldsymbol{x}) - \boldsymbol{\varepsilon}^{p,t+\Delta t}(\boldsymbol{x}) - \dot{\boldsymbol{\varepsilon}}^{p,t+\Delta t}(\boldsymbol{x}, \boldsymbol{\sigma}^{t+\Delta t})\Delta t]$$
$$\boldsymbol{\varepsilon}^{t+\Delta t}(\boldsymbol{x}) = \boldsymbol{C}^{-1} : \boldsymbol{\sigma}^{t+\Delta t}(\boldsymbol{x}) + \boldsymbol{\varepsilon}^{p,t+\Delta t}(\boldsymbol{x}) + \dot{\boldsymbol{\varepsilon}}^{p,t+\Delta t}(\boldsymbol{x}, \boldsymbol{\sigma}^{t+\Delta t})\Delta t \tag{1.21}$$

where $\boldsymbol{C}$ is the stiffness elastic tensor, $\boldsymbol{\varepsilon}$,$\boldsymbol{\varepsilon}^e$,$\boldsymbol{\varepsilon}^p$ are respectively the total, the elastic and the plastic strain tensor, and $\dot{\boldsymbol{\varepsilon}}^p$ is the plastic strain rate given by the Equation 1.18.

Now if we add and subtract to the stress tensor an appropriate $\boldsymbol{C}^0$, that is the stiffness of linear reference medium, multiplied for the displacement gradient tensor $u_{k,l}(\boldsymbol{x})$ we obtain

$$\sigma_{ij}^{t+\Delta t}(\boldsymbol{x}) = \sigma_{ij}^{t+\Delta t}(\boldsymbol{x}) + C_{ijkl}^0 u_{k,l}^{t+\Delta t}(\boldsymbol{x}) - C_{ijkl}^0 u_{k,l}^{t+\Delta t}(\boldsymbol{x}) \tag{1.22}$$

We can now reorder and regroup the previous equation obtaining

$$\sigma_{ij}^{t+\Delta t}(\boldsymbol{x}) = C_{ijkl}^0 u_{k,l}^{t+\Delta t}(\boldsymbol{x}) + \varphi_{ij}^{t+\Delta t}(\boldsymbol{x}) \tag{1.23}$$

where $\varphi_{ij}(\boldsymbol{x})$ is the so called polarization field and is given by

$$\varphi_{ij}^{t+\Delta t}(\boldsymbol{x}) = \sigma_{ij}^{t+\Delta t}(\boldsymbol{x}) - C_{ijkl}^0 u_{k,l}^{t+\Delta t}(\boldsymbol{x}) = \sigma_{ij}^{t+\Delta t}(\boldsymbol{x}) - C_{ijkl}^0 \varepsilon_{kl}^{t+\Delta t}(\boldsymbol{x}) \tag{1.24}$$

now if we combine the latter equation with the equilibrium hypothesis $\sigma_{ij,i}(\boldsymbol{x}) = 0$ we find

$$C_{ijkl}^0 u_{k,lj}^{t+\Delta t}(\boldsymbol{x}) = +\varphi_{ij,j}^{t+\Delta t}(\boldsymbol{x}) = 0 \tag{1.25}$$

if we now want to solve this differential equation for a periodic unit cell under an applied strain $\boldsymbol{E} = \langle \boldsymbol{\varepsilon}(\boldsymbol{x}) \rangle$ using the Green Function Method we need to write the following auxiliary equation

$$C_{ijkl}^0 G_{km,lj}(\boldsymbol{x} - \boldsymbol{x'}) + \delta_{im}\delta(\boldsymbol{x} - \boldsymbol{x'}) = 0 \tag{1.26}$$

where $G_{km}(\boldsymbol{x})$ is the Green Function associated with the displacement field $u_k(\boldsymbol{x})$. The solution for the displacement gradient is given by

$$u_{k,l}(\boldsymbol{x}) = \int_{R^3} G_{ki,jl}(\boldsymbol{x} - \boldsymbol{x'})\varphi_{ij}(\boldsymbol{x'})d\boldsymbol{x'} \tag{1.27}$$

The idea of utilizing FFT comes from the formulation of the micromechanical problem, which requires the computation of a convolution integral (see Equation 1.27) to resolve the displacement field of a nonlinear heterogeneous medium, which can be calculated as a convolution integral between GreenÕs function of a linear reference homogeneous medium and a polarization field. The advantage of which, enables this integral to be solved in Fourier space as just a product compared to a computationally intensive convolution integral which limits the efficiency of classical crystal plasticity approaches. The numerical approach, which is based on FFT method, requires a finite number of equally spaced frequencies, which can thereby account for transgranular misorientations. Due to the fact that the polarization field is unknown, an iterative procedure, consisting of an "augmented Lagrangian" scheme (basically requiring two auxiliary stress and strain-rate fields and will be described in the next section), is utilized to obtain a compatible strain-rate field and an equilibrated stress field. The simultaneous convergence of both, equilibrated and auxiliary stress fields, together with compatible and auxiliary strain-rate fields, guarantees the convergence of the model. We can solve Equation 1.27 in the Fourier space using the convolution theorem, and the compatible strain field deriving from the solution of Equation 1.25 is

$$\varepsilon_{ij}(\boldsymbol{x}) = E_{ij} + FT^{-1}[\mathrm{sym}(\hat{\Gamma}^0_{ijkl}(\boldsymbol{k}))\hat{\varphi}_{kl}(\boldsymbol{k})] \tag{1.28}$$

where the symbol "^" indicates the Fourier Transform and $\boldsymbol{k}$ is a frequency in the Fourier Space, and where $\hat{\Gamma}_{ijkl}$ is the Green operator in the Fourier space

that is given by the equation:

$$\hat{\Gamma}_{ijkl}(\boldsymbol{k}) = -k_j k_l \hat{G}_{ik}(\boldsymbol{k})$$
$$\text{with } \hat{G}_{ik}(\boldsymbol{k}) = [C^0_{kjil} k_l k_j]^{-1}$$

We should note that the Green operator is only a function of the frequency and of the stiffness reference tensor. It's evident that the most natural implementation of this formulation on a computer is done using the FFT algorithm, and is also obvious that the only error introduced so far is just due to numerical truncation during the calculation. Another thing that should be mentioned is, that while traditional FEM allows us to treat non periodic cells the CP-EVP-FFT formulation can be utilized with larger set of data without paying a high computational cost due to the high number of degree of freedom required by the former.

## 1.7 Hardening Law and the Iterative Procedure

Until now we have only taken into account the activity of the slip systems but we didn't talk about how to describe the strain hardening behaviour of the material: for this particular method we need to enter in the detail of the *Iterative Procedure* and this will be clear in a while. As in all equilibrium problems the criterion of minimization of energy must be fulfilled in order to find an equilibrated stress field that is compatible with a congruent strain field: to do this we need to introduce $\lambda^i_{ij}$ and $e^i_{ij}$ that are respectively an auxiliary guess stress and strain fields at iteration $i$. According to the method developed by Michel et al. [31] and Michel et al. [30] nullification of a residual $\boldsymbol{R}$, which is function of both auxiliary and solution stress and strain fields, is required. Defining the residual as difference between this two systems of fields

(and omitting the dependence from $\boldsymbol{x}$ to simplify the notation) we obtain:

$$\boldsymbol{R}_k(\boldsymbol{\sigma}^{(i+1)}) = \sigma_k^{(i+1)} + C_{kl}^0 \varepsilon_l^{(i+1)} - \lambda_k^{(i+1)} + C_{kl}^0 e_l^{(i+1)} \tag{1.29}$$

where we used the contracted index notation (i.e. $\sigma_{ij} \rightarrow \sigma_k$ with $k = 1, 6$). This nonlinear equation is solved using a Newton-Raphson like scheme:

$$\sigma_k^{(i+1,j+1)} = \sigma_k^{(i+1,j)} - \left( \frac{\partial R_k}{\partial \sigma_l} \bigg|_{\boldsymbol{\sigma}^{(i+1,j)}} \right)^{-1} R_l(\sigma(i+1,j)) \tag{1.30}$$

Now using the constitutive relation in Equation 1.21 and the Equation 1.29 with Equation 1.30 we will find a relation for the Jacobian, which can be written as a function of the variation of plastic strain rate over the variation of stress:

$$\frac{\partial R_k}{\partial \sigma_l} \bigg|_{\boldsymbol{\sigma}^{(i+1,j)}} = \delta_{kl} + C_{kq}^0 C_{ql}^{-1} + \Delta t C_{kq}^0 \frac{\partial \dot{\varepsilon}}{\partial \sigma_l} \bigg|_{\boldsymbol{\sigma}^{(i+1,j)}} \tag{1.31}$$

now the derivative on the right is the tangent compliance of Equation 1.18. For this we can find an approximate expression, neglecting second order terms that are a function of the CRSS, e.g. a function of the stress itself:

$$\frac{\partial \dot{\varepsilon}}{\partial \sigma_l} \bigg|_{\boldsymbol{\sigma}^{(i+1,j)}} \approx n \dot{\gamma}_0 \sum_{\alpha=1}^{N} \frac{m_q^\alpha m_l^\alpha}{\tau_0^\alpha(\boldsymbol{\sigma}^{(i+1,j)})} \left( \frac{\boldsymbol{M}^\alpha : \boldsymbol{\sigma}}{\tau_0^\alpha(\boldsymbol{\sigma}^{(i+1,j)})} \right)^{n-1} \tag{1.32}$$

Once convergence is achieved on $\boldsymbol{\sigma}^{(i+1)}$ the new guess for the auxiliary system is:

$$\boldsymbol{\lambda}^{(i+1)}(\boldsymbol{x}) = \boldsymbol{\lambda}^i(\boldsymbol{x}) + \boldsymbol{C}^0 : \left( \boldsymbol{e}^{(i+1)}(\boldsymbol{x}) - \boldsymbol{\varepsilon}^{(i+1)}(\boldsymbol{x}) \right) \tag{1.33}$$

Looking at Equation 1.32 and at the overall iterative procedure it's easy to see how this method allows us to choose different type of hardening laws. The hardening law implemented in the CP-EVP-FFT is a *Generalized Voce's Hardening Law* (Tome et al. [60]) of the type:

$$\tau^\alpha(\Gamma^\alpha(\boldsymbol{x}, t)) = \tau_0 + (\tau_1 + \theta_1 \Gamma^\alpha(\boldsymbol{x}, t)) \left[ 1 - \exp\left( \frac{-\Gamma^\alpha(\boldsymbol{x}, t)\theta_0}{\tau_1} \right) \right] \tag{1.34}$$

where $\tau$ is the RSS and $\Gamma$ is the accumulated strain and the physical meaning of all the parameter of this equation is shown in Figure 1.11.

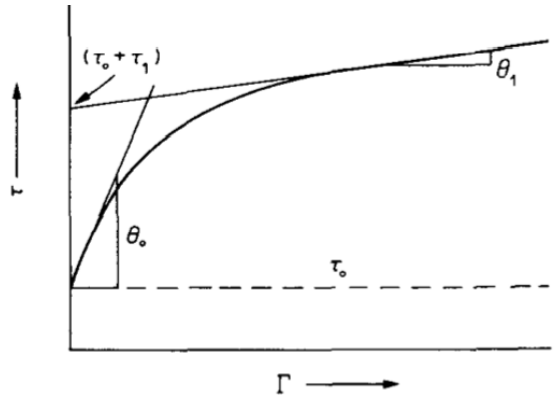


**Figure 1.11:** Physical meaning of Generalized Voce's Hardening Law

## 1.8 Boundary Conditions

The last ingredient that we need to complete the formulation of CP-EVP-FFT model, is the formulation of the Boundaries Conditions. The algorithm described above solves a problem of imposed strain of the type:

$$E_{ij} = E_{ij}^{t} + \dot{E}_{ij}\Delta t \tag{1.35}$$

the code implement a set of mixed condition. We can force either stress, strain rate or an compatible combination of them. To do this an extra step is required after that $\boldsymbol{\lambda}^{(i+1)}$ (see Equation 1.33) has been determined. Let's define the imposed macroscopic stress tensor $\Sigma$: if $\Sigma_{pq}$ is imposed, the corresponding guess for the strain component $E_{pq}^{(i+1)}$ is obtained, according with Michel et al. [31], as:

$$E_{pq}^{(i+1)} = E_{pq}^{(i)} + (C_{ijkl}^{0})^{-1}\alpha^{[kl]}\left(\Sigma_{kl} - \langle\lambda_{kl}^{(i+1)}(\boldsymbol{x})\rangle\right) \tag{1.36}$$

where $\alpha^{[kl]}$ is a parameter that is equal to 1 if $\Sigma_{kl}$ is imposed and zero otherwise.

As previously discussed in this section, one of the advantages of CP-EVP-

FFT is the direct use of information from crystallographic characterizations technique, such as EBSD or HEDM, because, by construction, the CP-EVP-FFT approach is a mesh-free formulation. In contrast to FEM methods, which utilize conform meshes (i.e. smooth grain boundaries), the CP-EVP-FFT introduces stair-stepped GBs. The difference in full field results between these two different approaches has been investigated by Kanit et al. [22] and did not display appreciable differences.

## 1.9 Utilizing CP-EVP-FFT

### 1.9.1 Input

The CP-EVP-FFT requires different input:

1. a file containing each position in the crystal (x,y,z), $Bunge_{c\rightarrow s}$ orientation angles, grain which it belongs, and phase (for instance there could be gas e.g. voids).

2. a file specifying the elastic macroscopic properties: stiffness matrix for cubic materials or Young Modulus and Poisson Ratio for isotropic materials.

3. a file with single-crystal plastic parameter: material unit cell type, the slip system that must be taken into account (i.e. $\langle 111\rangle[110]$ for FCC ), all the 4 Generalized Voce's Law hardening parameter as discussed in Equation 1.34 (e.g. the hardening exponent, the reference strain rate at which the hardening parameters have been estimated, and self and latent hardening coefficient).

4. and, of course, a file including the boundary and initial conditions: i.e. for a simple tensile test with imposed a macroscopic strain rate along the Z axis (that in our notation is identified by the subscripts 33 in tensorial

notation or by the the third component of the vector if the Voigt [3] notation is used) we will set $\dot{E} = [-0.35, -0.35, 1, 0, 0, 0]$ with also a tensor, that we will call $\dot{E}_{know,unknown}$ that specify which of these condition is imposed and which is just an initial value, that will be $\dot{E}_{know,unknown} = [0, 0, 1, 1, 1, 1]$ for our example where 1 means constrained and 0 means initial values; also we need to constrain the macroscopic stress in the same way: $\Sigma = [0, 0, 0, 0, 0, 0]$ with $\Sigma_{know,unknown} = [1, 1, 0, 0, 0, 0]$. In practice we are telling the code that, at macroscopic level, only the $E_{11}$ and $E_{22}$ are not constrained, this allow to the specimen the possibility to arrange the macroscopic in such a way to accommodate for the Poisson Effect. Also we need also to specify the time-step, that must be chosen not too large such that the code can reach convergence, and the number of steps that multiplied for the strain rate will define the final strain reached. Also we must specify the tolerance between two iterations to allow the code to advance to the next time-step.

5. optionally an initial hydrostatic stress state can be inserted.

### 1.9.2 Output

The output of code are a set of files

1. a file containing the macroscopic response of the polycrystal: strain, plastic strain, stress and the normalized stress (which is the stress divided the volume fraction of the solid phase).

2. a file containing the reoriented texture (polycrystals material rearrange the orientation of grains during loading to minimize the energy).

3. a file for each of the subsequent tensorial quantity at each point of the grid: strain, displacement, elastic strain, stress and normalized stress.

[3] **Note:** all this tensor are expressed w.r.t. Voigt notation: $V = [V_{11}, V_{22}, V_{33}, V_{23}, V_{31}, V_{12}]$

4. and other files containing errors at each iteration, the number of steps required for the convergence at each time-step.

## 1.10 Crystallographic Modeling of Polycrystal

### 1.10.1 EBSD scan and 3D Texture Reconstruction

Electron BackScatter Diffraction (EBSD) is a characterization technique which is many times used in conjunctive with crystallographic modeling to obtain the orientation of a crystal belonging to an aggregate (the schematic of the experiment is given in Figure 1.12). Essentially the sample is placed in a Scan-

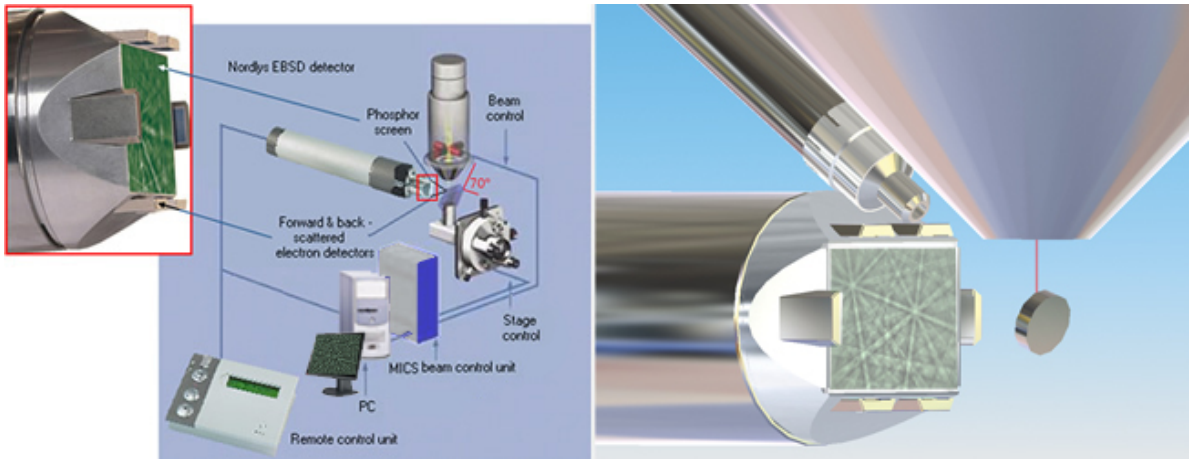


**Figure 1.12:** on the left EBSD experiment setup, on the right the projection of the EBSD pattern on the phosphor screen (image from EBSD.com [12])

ning Electron Microscope (SEM) with an angle of circa 70° between itself and the accelerated electron beam, the atomic plane can diffract electrons that can be detected when they hit the phosphor screen generating visible lines. Each atomic plane diffracts electrons in a cone (see Figure 1.13), and due to the fact that the electrons beam interact not only with atoms on the surface, Kikuchi band are formed, and the width of this band is proportional to the distance between 2 parallel atomic planes. The result of this experiment can be seen in Figure 1.14(a) where each Kikuchi band has its own direction superimposed. Furthermore, it should be noted that the intersection between Kikuchi bands identify the common crystallographic direction of the intersecting plane. Also, for a better physical understanding of the EBSD Pattern, in Figure 1.14(b) an FCC unit-cell is superimposed. It's obvious that different oriented crystal

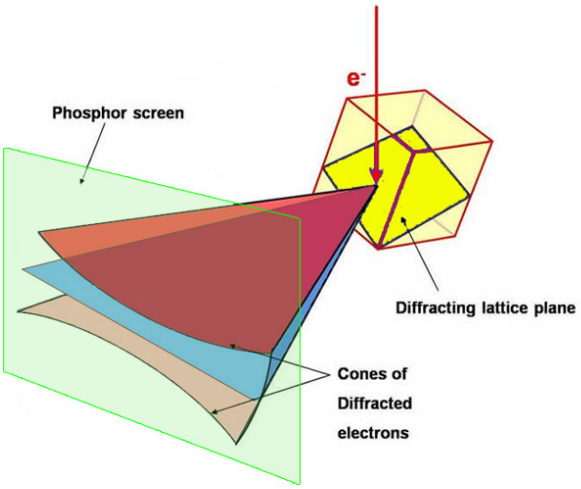


**Figure 1.13:** how atomic planes diffract electrons (image from EBSD.com [12])

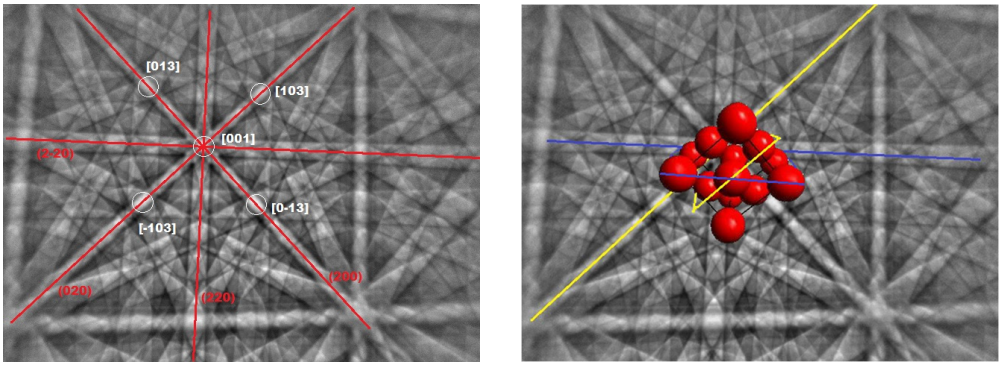


(a) EBSD Pattern with miller indexes of planes and directions

(b) EBSD Pattern with a superimposed FCC unit cell

**Figure 1.14:** images from EBSD.com [12]

produce a different pattern, also different material even if with same unit-cell does, due to the difference between parallel plane spacing. Depending on how the pattern is oriented looking for precise point, we can easily calculate the crystal orientation.

Now that we know how to obtain the orientation of a layer of a polycrystal, we can imagine repeating the same operations many time and obtain a 3D texture of the entire specimen: the problem of reconstructing the the entire mesh arise. To do this we use a software called *Dream3D* (BlueQuartz [8]) with his data-sample: a real Nickel-based super alloy 3D EBSD scan dataset

called *SMALL IN100*. This software has the capability of, given an input of organized series of EBSD scan file, reconstruct the entire three dimensional texture following the steps:

- realigning each layer of material using the misorientation angle tolerance (see Equation 1.37)
- divide the aligned texture in grains also using misorientation angle (grains are defined as portion of material with the same orientation, from an engineering point of view we set a misorientation tolerance that usually is 2°(see Equation 1.37))
- create easy to read, understand, and use files with all the crystallographic properties at each point in the grid such as orientation, grain number, Inverse pole figure color and much more.

The misorientation angle $\Theta$ is defined as follow:

$$\Theta = \min \left| cos^{-1} \left( \frac{\text{trace}(\boldsymbol{O}_{432} \Delta \boldsymbol{g}) - 1}{2} \right) \right| \tag{1.37}$$

where $\boldsymbol{O}_{432}$ is the simmetry opreator which acount for all possible simmetrical orientation, $\Delta \boldsymbol{g} = \boldsymbol{g_1}^{-1} \boldsymbol{g_2}$ in which the subscript 1 and 2 indicated to different adjoining point in the grid (see Figure 1.15).

It's also to note that Dream3D has much more features that can be used for texture manipulation such as volume cropping, creation of statistically equivalent texture (e.g. given an *Orientation Distribution Function*(ODF), a texture with the same ODF can be artificially created), calculation of many interesting parameter like Schimd Factor, Quaternion and Eueler angles etc. The output files generated by Dream3D are vtk (see vtk.org [62] to understand how a vtk file is organized and how can be written and manipulated) and csv format. The data that comes from this files can be read and reorganized to match the input file format of CP-EVP-FFT code: at this point we are ready to run our simulations.

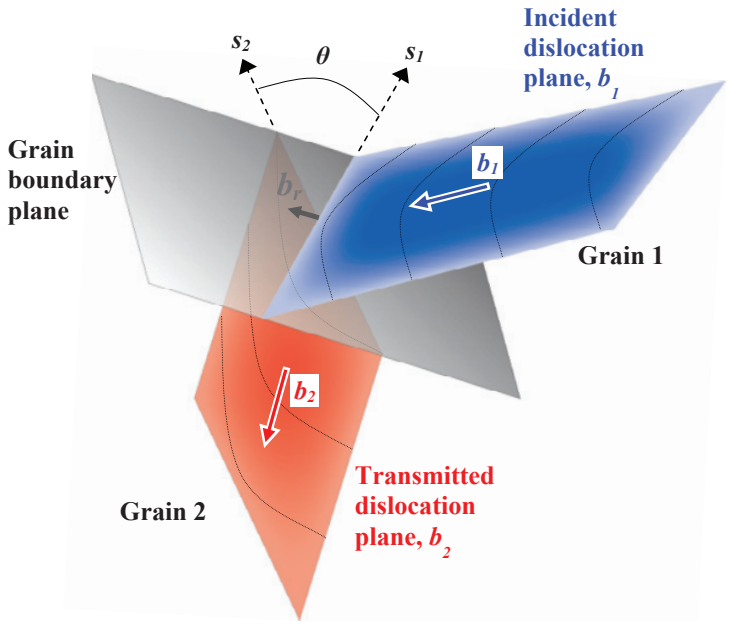


**Figure 1.15:** Schematic of slip transmission through a grain boundary. **b1** and **b2** are the Burgers vector of the incident and transmitted dislocations across the GB plane. $\Theta$ is the angle between the lines of intersection between slip planes of the incident and transmitted dislocations and the GB plane (see Equation 1.37). **br** is the residual dislocation left in the GB plane (image from Abuzaid et al. [2]).

The subsequent step is the data visualization. The software that we decide to use for this scope is called *ParaView* (paraview.org [41]) that is an open-source, multi-platform data analysis and visualization application. It can use many different type of input formats: to maintain some sort of coherence we used vtk file. This means that all the output data coming from CP-EVP-FFT code have been reorganized in vtk format[4].

### 1.10.2 Grain Boundaries Identification and visualization

Before showing some simulation results as proof of the work done there is another thing to note: even if CP-EVP-FFT use a phenomenological approach we are dealing with a polycrystal approximation: this means that the grain boundaries, even if not explicitly defined, should play some role in the stress field distribution. This lead us to find a way to identify the location

[4]**Note:** all the routine needed to go from Dream3D to CP-EVP-FFT, from the CP-EVP-FFT to ParaView and other data manipulations have been written in Matlab

of boundaries in such a way that we can easily superimpose it to the stress field. Starting from the fact that we know for each point in the FFT grid the grain it belongs[5], that from now on we will call this *Grain Id*, the obvious way to proceed is to set some control point: thinking to a point in the grid as a cube with uniform characteristic we can set 3 different control point that will be computed in cascade to determine the boundaries profile. Looking at

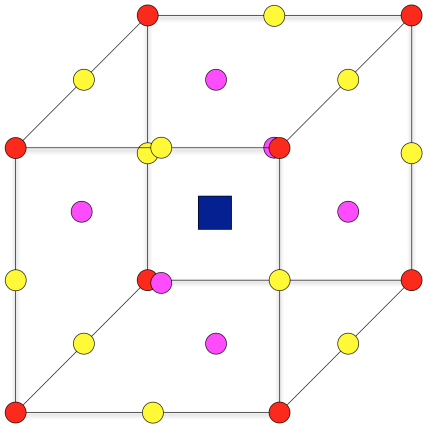

**Figure 1.16:** image of the control points used for to create the boundaries image

Figure 1.16 the blue square represents the Grain Id of the volume, the 6 purple circle represent the directions of the $1^{st}$ comparison and they will be set to 0 if that point are boundaries 1 otherwise (this operation check a direction at time x,y,z); the $2^{nd}$ operation is to check on the $xy$, $xz$ and $yz$ directions: these point are set to 1 only if they are inside a square of non boundaries; the $3^{rd}$ the red circle represent the check on the $xyz$ direction and as before the are non boundaries only if inside a cube of non boundaries point. A high efficiency and parallel algorithm has been written to perform the boundaries check of a simulation with a very large number of elements.

We should also note, that to perform this operation, we have to refine the entire texture: i.e. if we start for example with a 32x32x32 texture the boundaries requires a 63x63x63 points (the ones at end of the domain remain

[5]**Note:** the grain segmentation has been performed by Dream3D utilizing the misorientation criteria

pinned).

# Chapter 2

# The short crack growth problem

The case of short cracks is one of the most well known since Paris' law (Equation 2.1) can significantly underestimate their rate of growth, and the large number of ad-hoc laws reflect the fact that there is not a single type of short-crack deviation. Some authors have suggested a classification of cracks (see Suresh and Ritchie [58], Ritchie and Lankford [45], Miller [33]) as follows:

- microscopic short crack (microstructurally small) for which continuum mechanics breaks down and microstructural fracture mechanics is needed, see for example the model of Navarro and de los Rios [38]; this is perhaps the most complex category, since crack deceleration or self-arrest is very dependent on the grains size and orientations, and possible decelerations or "minima" in $da/dN$ and multiple small-crack curves can be found (Ritchie and Lankford [46]). This is the object of the present work.

- physically small crack (mechanically small) compared to the scale of local plasticity, for which Elastic-Plastic Fracture Mechanics (EPFM) is needed, first introduced by Tomkins in 1968 (see Miller [33]) who equated $da/dN$ to crack tip decohesion (from knowledge of the cyclic stress-strain curve), and thence to the bulk plastic strain field that occurs, for example, under high strain fatigue.

- macroscopic long crack, growth phase described by Linear Elastic Fracture Mechanics (LEFM).

Figure 2.1 shows the visualization of the transition between microstructurally small crack and physically small crack and the definition of $\Delta K_T$ .

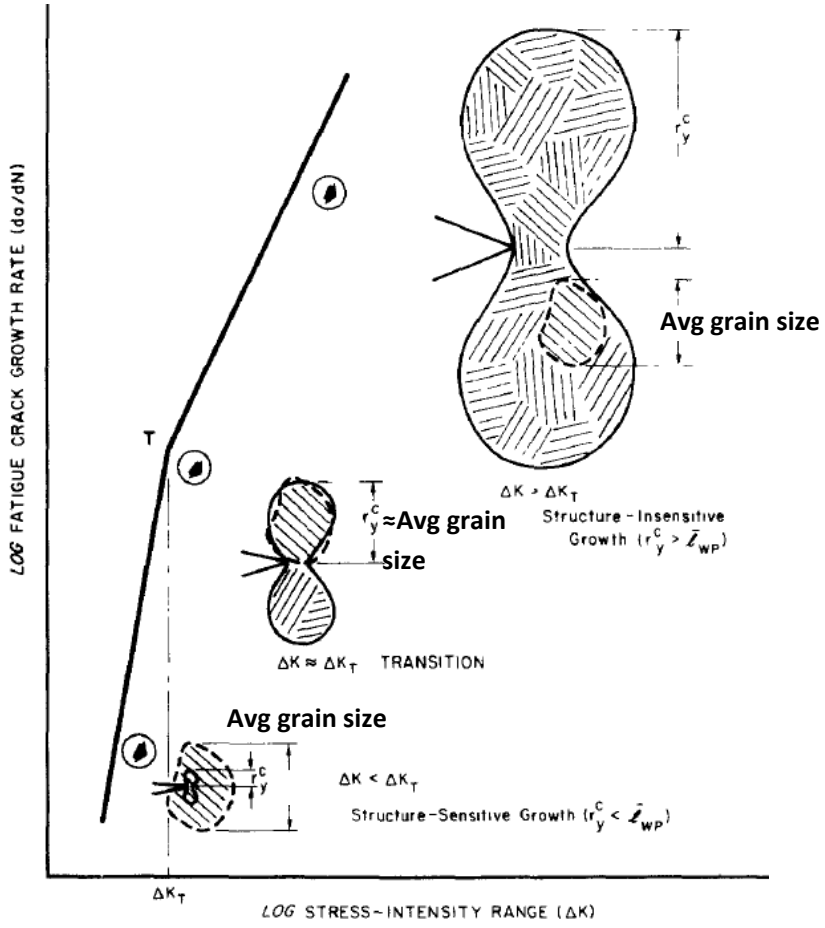


**Figure 2.1:** Schematic representation of the plastic zone size vs average grain size and their grwoth rate: (a) microstructurraly short crack in witch structure-sensitive behavior is observed (reversed plastic zone < average grain size); (b) transition between structure sensitive/insensitive behavior ($\Delta K = \Delta K_T$); (c) physically small crack (reversed plastic zone > average grain size) in which structure-insensitive behavior is observed (image from Yoder et al. [64])

## 2.1 Litetature review and state of the art

The Paris' law (see Equation 2.1) for fatigue crack growth considers long crack, defined when the material can be considered homogeneous and the plastic zone ahead of the crack tip is small compared to the characteristic length of the specimen (Paris et al. [42]).

$$\frac{da}{dN} = C\Delta K^m \tag{2.1}$$

where $a$ is the crack length,$N$ the number of cycle, $C$ and $m$ material parameters, and $\Delta K$ is the range of stress intensity factor, i.e. the difference between the stress intensity factor at maximum and minimum loading, which is a function of:

- range of applied stress $\Delta\sigma$;
- the geometry of the component;
- crack length $a$;

and its general formulation is

$$\Delta K = \Delta\sigma Y\sqrt{\pi a} \tag{2.2}$$

where $Y$ is a dimensionless parameter that account for the geometry of the component. Furthermore, due to the size of the crack, characteristic values of the stress intensity factor for the short crack growth problem are found in *stage I* of the Paris' diagram (see Figure 4.13)

Short crack growth is significantly influenced by the microstructure of the material, in fact, at very low $\Delta K$ levels, the fracture surface micromorphology has shown to posses a highly faceted texture and multiple crack paths (see Figures 2.2 and 2.3 ). This influence needs to be quantified for accurate life prediction.

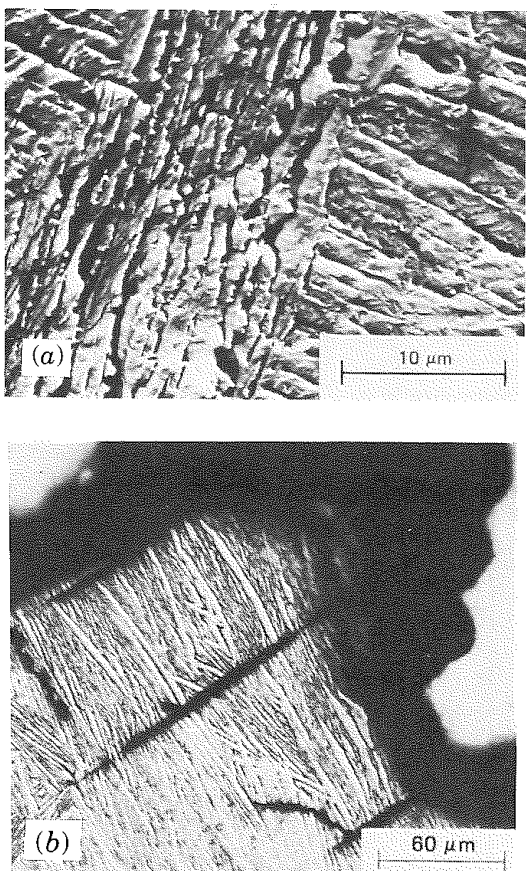


**Figure 2.2:** Fatigue crack surface micromorphology in Titanium based alloy: (**a**) faceted surface; (**b**) multiple crack path at $\Delta K < \Delta K_T$ (images from Yoder et al. [64])

The first authors to investigate microstructural short crack growth (for brevity we will refer to it as SCG) were McEvily and Boettner [29], specifically observing that the short crack growth rate is dependent on grain orientation and can be idealized as a series of slip process Figure 2.4. Short crack advancement can be idealized as series of slip processes (Neumann [39]), with the criterion for dislocation emission from the crack tip outlined by Rice and Thomson [44] (see Figure 2.5). Subsequently Yoder et al. [64] investigated the influence of grain size in variability of the stress intensity factor threshold value ($\Delta K_{th}$ )in polycrystalline material, finding that it increases proportionally to the square root of the average grain size (see Figure 2.6). Navarro and de los Rios [38] proposed a model for SCG in which they assumed that the extent of

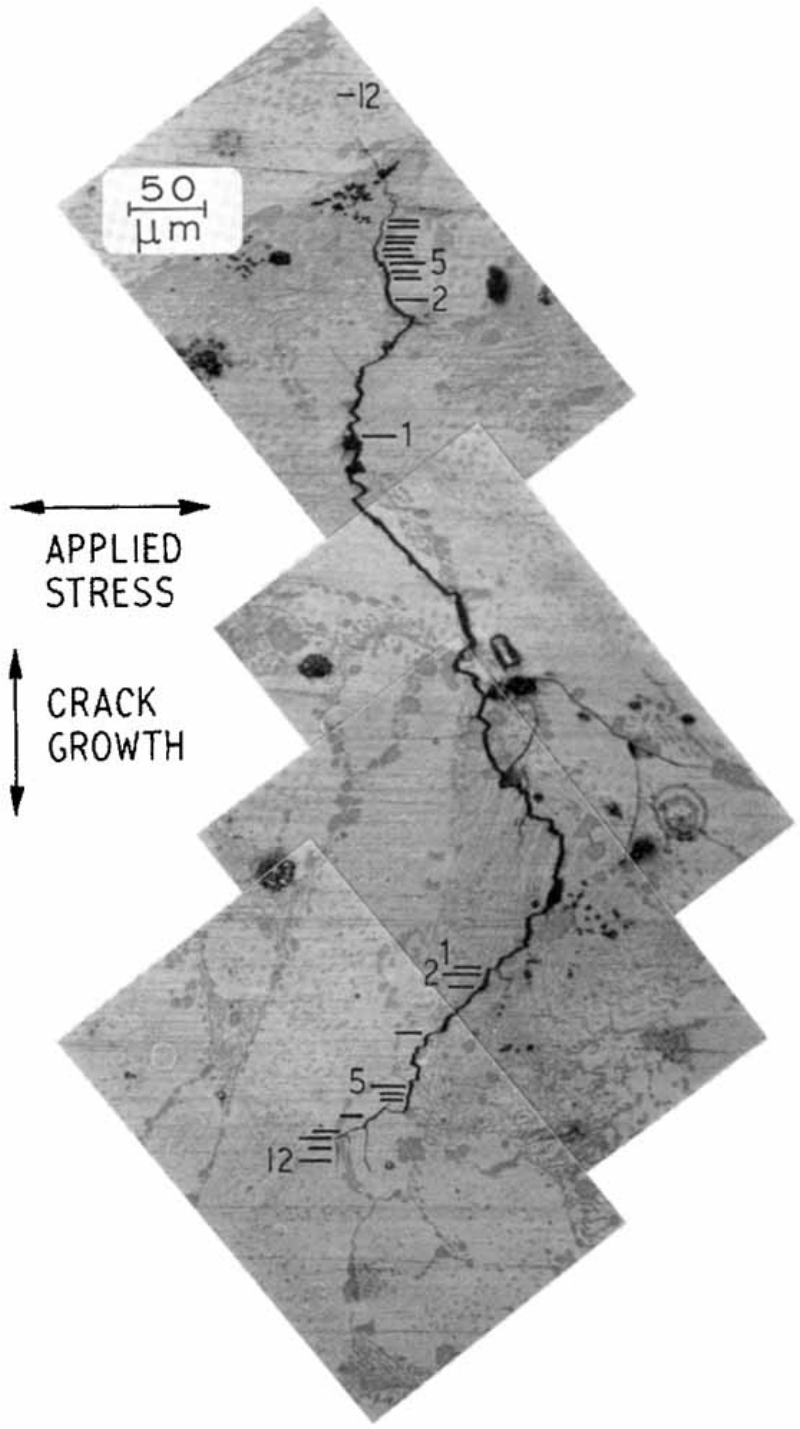


**Figure 2.3:** Surface view of a semi-elliptic crack. The crack path is influenced by microstructure features like grain boundaries (image from Taylor and Knott [59])

the plastic zone ahead of the crack tip is confined at the first obstacle for dislocation motions, i.e. grain boundaries (GBs), and that growth rate depends

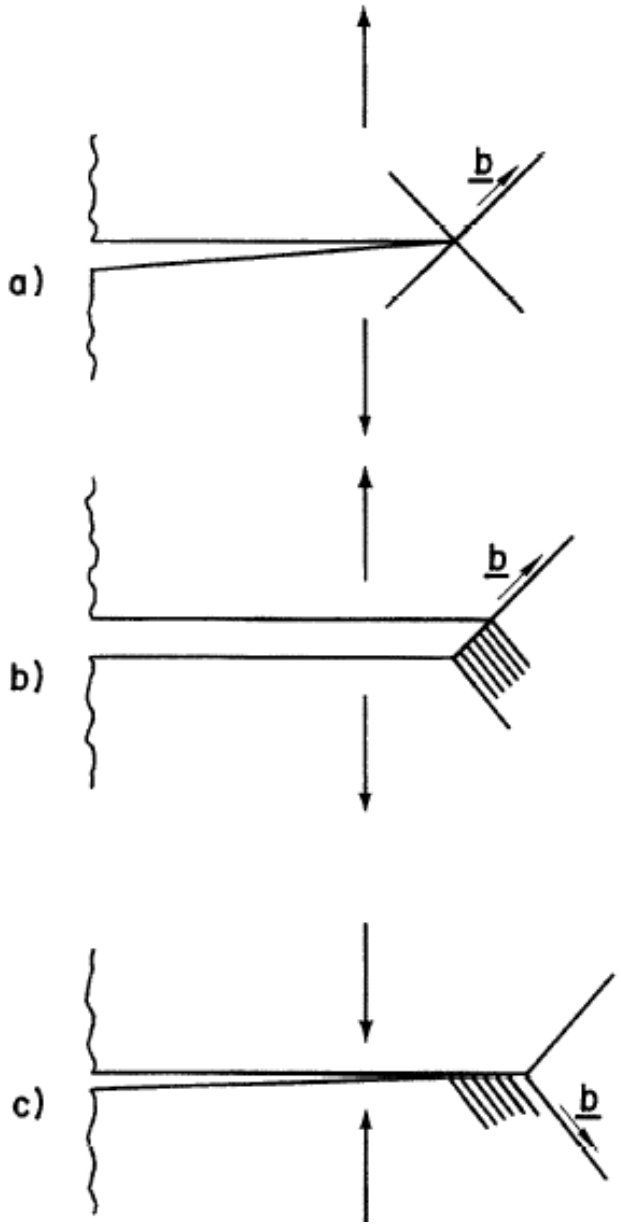


**Figure 2.4:** Schematic model of crack growth at mesoscopic scale. Burgers' vector indicate sequence of operative slip system (image from McEvily and Boettner [29])

on the distance between the crack tip and the obstacle itself. These studies suggest that microstructural parameters, like i.e. grain orientation, grain size, distance of the crack-tip from obstacles, etc., strongly influence the SCG rate (see Figure 2.7). Further, since each engineering alloy posses a distribution of microstructure attributes, these features play a crucial role of microstructure

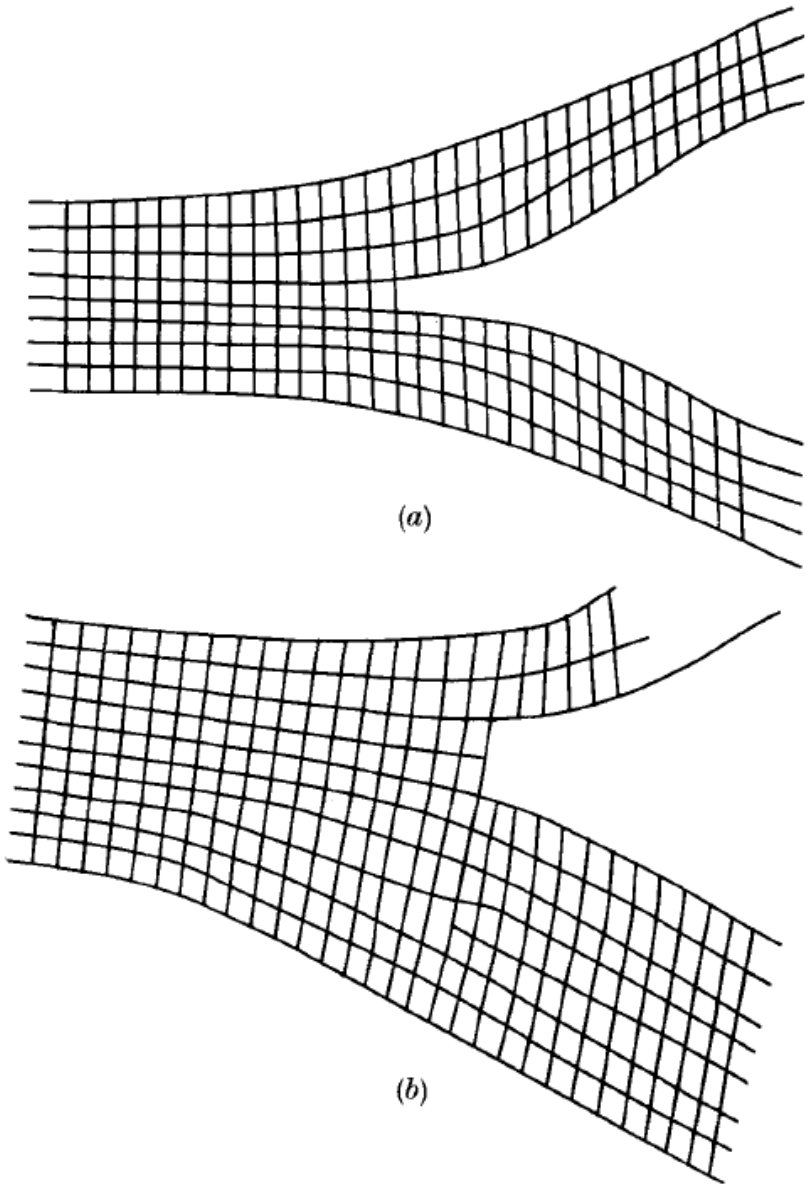


**Figure 2.5:** Schematic model of crack growth at atomistic scale. An atomically sharp crack is blunted when a dislcoation is emitted from the tip when the Burgers' vector has a normal component to the fracture plane (image from Rice and Thomson [44])

variability in the SCG behavior of the material. The aim of the present work, and also its novelty, is to investigate the relationship between microstructure

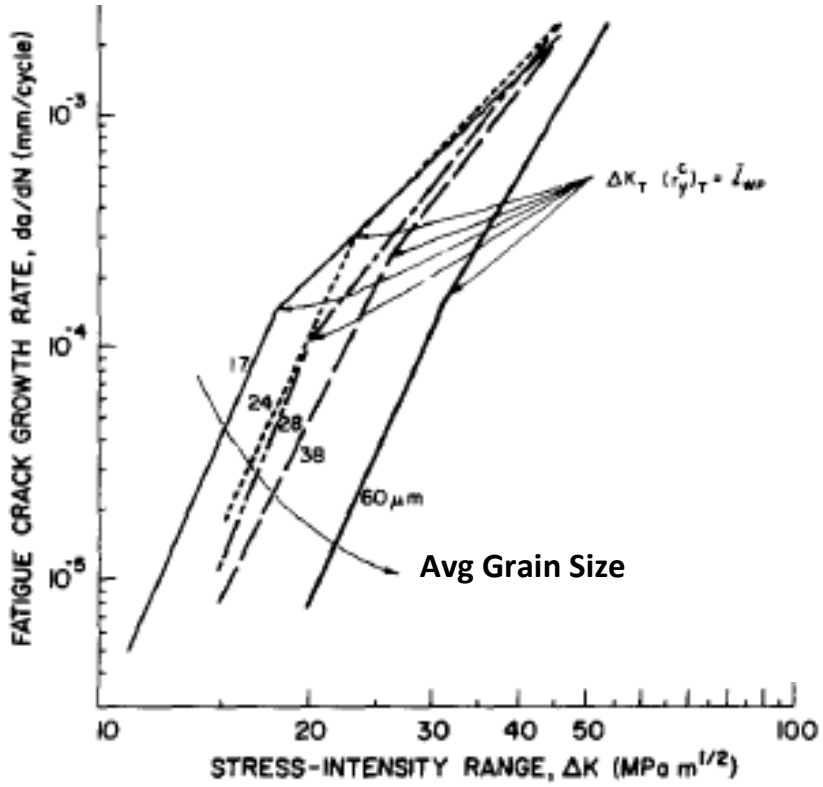


**Figure 2.6:** Dependance of short crack growth rate from the average grain size image from Yoder et al. [64]

variability and SCG in complex situation using high-resolution simulations, to achieve a better insight into the driving force behind short crack propagation. The advent of powerful microstructural-sensitive computational tools namely crystal plasticity (CP) (Asaro [5]) allowed researchers to investigate the relationship between SCG and microstructure parameters. Wilkinson [63] studied the interaction between the relative position between the crack-tip and GBs distance building on the model proposed by Navarro and de los Rios [38]; the results showed that while the crack is in the core of a grain, the growth rate is almost constant and as the crack impinges upon a GB, the growth rate is dependent on the neighboring grain's misorientation. Many other authors implemented CP simulations on simplified microstructures, in which all these studies converge to similar coherent solutions, ( i.e. Ferrie and Sauzay [14], Potirniche et al. [43], and serve as the basis for understanding complex

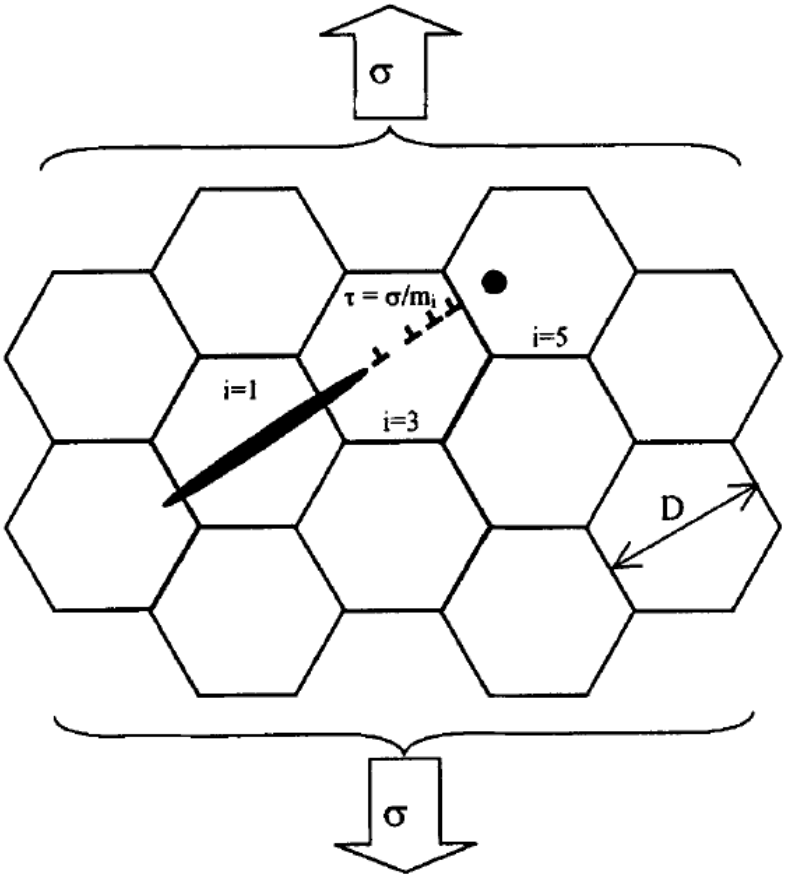


**Figure 2.7:** Schematic of model for dislocations pile-up at the first grain boundary proposed by Navarro and de los Rios [38] (image from Wilkinson [63]).

SCG behavior. Many of the aforementioned studies, in order to find distinct relationships, account for 1 or 2 microstructure parameter, thus limiting the exploration of the complete space of complex 3D behavior and not accounting for concepts involving the interaction of multiple microstructure attributes, such as grain clustering. Grain clustering serves as an important feature for fatigue analysis (Guilhem et al. [18], Sangid et al. [52]). To achieve a better understanding of the physics behind SCG, many researchers investigated the role of dislocations. Experiments conducted by George and Michot [16] show that the most common source of dislocation at the crack-tip, is a source which emits multiple Burger vector on different glide planes simultaneously. To simulate this behavior, many researchers have utilized molecular dynamic (MD)

simulations. Bitzek and Gumbsch [7] and Zhang and Ghosh [65] investigated the dependence of dislocation emission, multiplication and interaction at the crack-tip within a single crystal. These simulations depicted the importance of dislocation type and crystal orientation on crack growth. Moreover Sangid et al. [51] investigated the role of GBs in slip transmission and dislocation nucleation, observing that the character of GBs introduce variability in the response of the material. All these behaviors need to be taken into account to predict material performance during SCG in polycrystalline materials, which is the aim of this study. Each of the microstructure attributes influences SCG, albeit engineering materials exhibit a distribution of microstructural features; in order to quantify the variability introduced by the microstructure, we first discuss damage induced during crack growth. Mughrabi [37] related SCG rate to irreversible plastic strain accumulation during cyclic loading. According to this idea of damage, but independently Bennett and McDowell [6], investigated a nonlocal metric based on work of Fatemi and Socie [13] that account for the importance of the normal stress on the critical slip plane. The Fatemi-Socie parameter has been defined as a fatigue indicator parameter (FIP), which has been recently correlated to crack tip displacement by Castelluccio and McDowell [11]. Based on analysis, Hochhalter et al. [20] investigated the different possible formulations of FIPs. The results found an equivalence of the FIPs in crack behavior and asserting that the FIPs can be used for fatigue-life prediction. In this work, we will correlate the variability in FIP parameters in the vicinity of the crack-tip to the variability experienced by the stress intensity factor threshold ($\Delta K_{th}$ ) in stage 1 of crack propagation. The need to address microscopic variability is critical, in order to understand SCG and ascertain its driving force, the results have the potential to more accurately predict fatigue life. Due to the complexity of this topic, many authors in recent years have focused their research on specific microscopic features, in order to provide the foundations for a more complete understanding. But this approach cannot handle the complex interactions between microstructural attributes that are

present at the crack tip. In this work, we will use a real microstructure with a very high resolution discretization grid to investigate the local influence on variability and show how the change of one parameter will influence the behavior ahead of the crack tip. Subsequently, in order to mimic SCG, we will perform quasi-static analysis of advancing crack lengths. We will also show how the crack path is related to extreme values in the FIP fields and how the clustering effect is a crucial parameter in SCG. This work is organized as follows. In Chapter 3 covers, simulations, material parameters, and crack geometry. Chapter 4 is dedicated to the results and discussion: in section Section 4.1, we investigate variability in the macroscopic material response; section Section 4.2 is dedicated to slip-system variability investigation ahead of the crack-tip; in Section 4.3, we define FIPs and discuss their behavior on SCG; and, finally, in Section 4.4, we discuss the analogy between the variability in the FIPs and SCG. In Chapter 5, we draw conclusions about this study.

# Chapter 3

# Simulation setup and crack design

The microstructure that we use for our analysis is a freely available 3D EBSD dataset of IN100 sample performed using a dual beam FIB with a resolution of 0.25 $\mu m$. To achieve high-resolution analysis, after microstructure reconstruction performed with Dream3D, we extracted a cubic subset of $32^3$ voxels from the IN100 dataset (AFRL-WPAFB [3]). The subset was subsequently refined to $128^3$ voxels, thus reaching a resolution of 0.0625 $\mu m$. During the refinement operation, EBSD results have been maintained constant (the 64 voxels resulting from the refining procedure have the same parameters of the original voxel). The result of this cropping operation is a non-periodic unit-cell. The CP-EVP-FFT operation requires periodic microstructure and boundary conditions, which are circumvented by adding a gas phase (infinite compliance, e.g. zero stress), in such a way to obtain a cylinder of solid material, as shown in Figure 3.1. It should be noted that our analysis is mediated by slip-based deformation confined to the primary octahedral slip systems within the simulations (namely $\{111\}\langle 110\rangle$), which is the primary mechanism for short crack growth (SCG) in FCC materials, as pointed out by [29]. To describe the IN100 elasticity behavior, we modeled it as cubic material, e.g. three unique constants describing its elastic response. The single crystal stiffness constants used in this work are obtained from experiments by [55]. For the material's

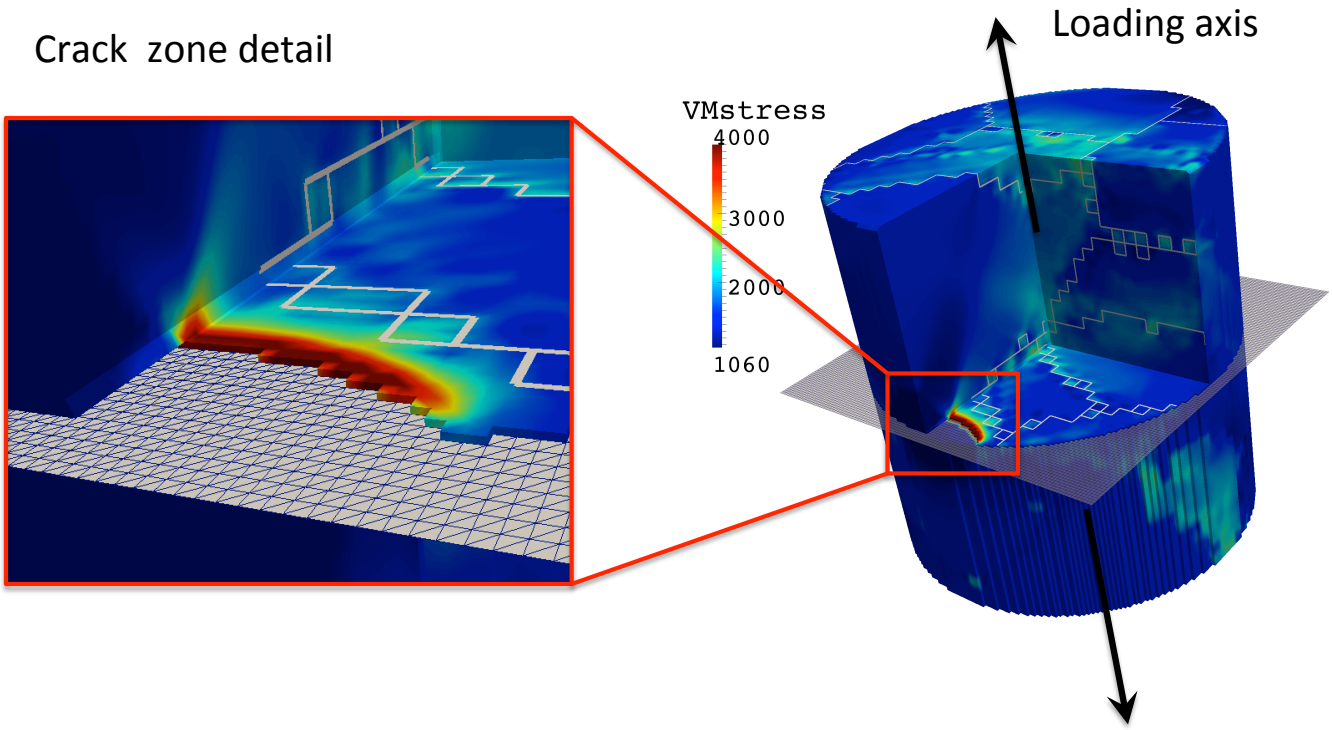


**Figure 3.1:** Overview of the Von Mises equivalent stress distribution. The loading axis and crack are denoted. The shaded plane is the crack plane. Note that this picture has been taken at 0.88% strain

plastic response, the Voce's hardening parameters for single crystal behavior were fit for a uniaxial tensile strain range, $0 - 10\%$, obtained at $650°C$ at a strain rate of $8.33 * 10^{-5} \quad s^{-1}$ (Fromm et al. [15]). The hardening response was fit in the CP-EVP-FFT model for an uncracked microstructure with uniaxial loading aligned to the longitudinal axis of the cylinder, as shown in Figure 3.1. The resulting numerical values of material fitting parameters utilized for all the simulations are shown in Table 3.1.

| **Elastic Constants** $[MPa]$ |
|---|
| $C_{11} = 158860$ |
| $C_{12} = 73910$ |
| $C_{44} = 130150$ |

| **Voce's Hardening Parameters** $[MPa]$ |
|---|
| $\tau_0 = 485.23$ |
| $\tau_1 = 38$ |
| $\theta_0 = 1000$ |
| $\theta_1 = 456$ |

**Table 3.1:** Elastic Constants and Voce's parameter in common through all the simulations

We also analyzed norm2 error between simulations containing $32^3$, $64^3$, and $128^3$ voxels, by using the Von Mises equivalent deviatoric stress fields, the results showed that at the higher resolution the $norm2$ error is lower than 5%. Furthermore, we analyzed the effect of the two non-periodic boundary surfaces; Rollett et al. [47] pointed out that a lack or an excess of stress at the edges suggest that high or low stresses are not introduced by the non periodic microstructure. According to their finding, we note that a small gradient in the stress field has been introduced in these zones, but it is rapidly decreasing moving away from boundary surfaces (2 or 3 voxels in all directions in the most refined grid, depending on the microstructure) and does not interact with the strain fields produced in our area of interest. In our analysis, we are interested in a restricted volume surrounding the crack-tip that introduce much higher gradients and values in both stress and strain fields. To catch quasi-static SCG behavior in a cylindrical specimen, elliptic cracks of different lengths have been inserted in the middle plane of the specimen substituting material phase with gas phase (see Figure 3.2 for crack geometry detail and Table 3.2 for the crack parameters); it should be noted that the smallest crack (namely the one with length $a = 0.66 \quad \mu m$ is completely embedded inside a single grain (from now on we will call this the cracked grain).

| **A** $[Voxel]$ or $[\mu m]$ | **B** $[Voxel]$ or $[\mu m]$ | **a** $[Voxel]$ or $[\mu m]$ |
|---|---|---|
| 12 or 0.75 | 20 or 1.25 | 10.5 or 0.66 |
| 16 or $1,00$ | 24 or 1.50 | 14.5 or 0.91 |
| 20 or 1.25 | 28 or 1.75 | 18.5 or 1.16 |
| 28 or 1.75 | 36 or 2.25 | 26.5 or 1.66 |
| 48 or 2.75 | 52 or 3.25 | 42.5 or 2.66 |

**Table 3.2:** Crack parameters

Also to address variability at the crack tip due to grain reorientation (see Figure 3.3 ) the cracked grain has been randomly reoriented in six distinct simulations. Please refer to the inverse pole figure (IPF) in Figure 4.1 for the orientations of the original and six randomly oriented cracked grains. As

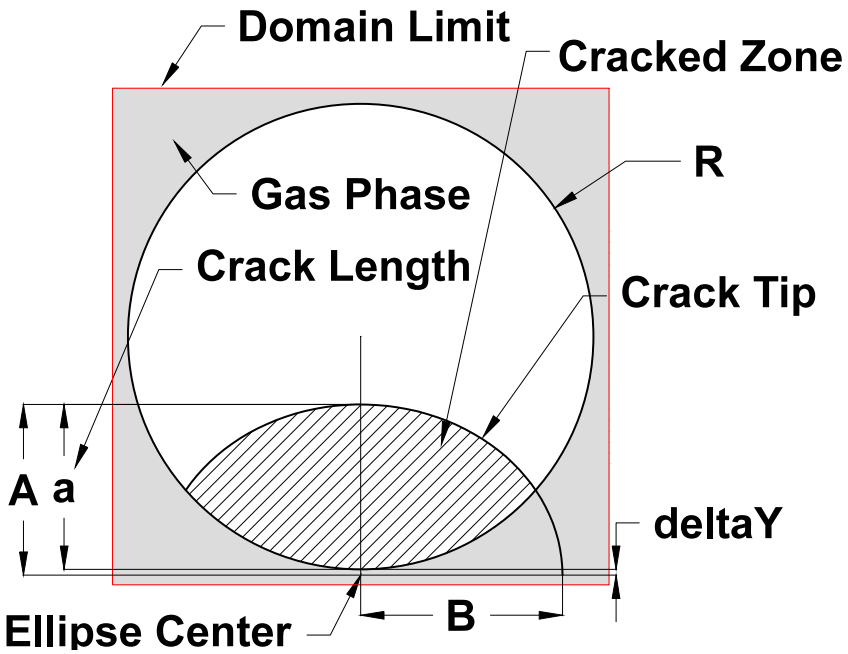


**Figure 3.2:** Schematic of crack geometry illustrating all the parameter used to build the crack. Common parameters for all the simulation and realizations are $R = 60$ $[Voxel]$ or 3.75 $[\mu m]$; $deltaY = 1.5$ $[Voxel]$ or 0.094 $[\mu m]$

a result, 35 simulations have been analyzed containing a combination of 7 orientations of the cracked grain with 5 crack lengths.

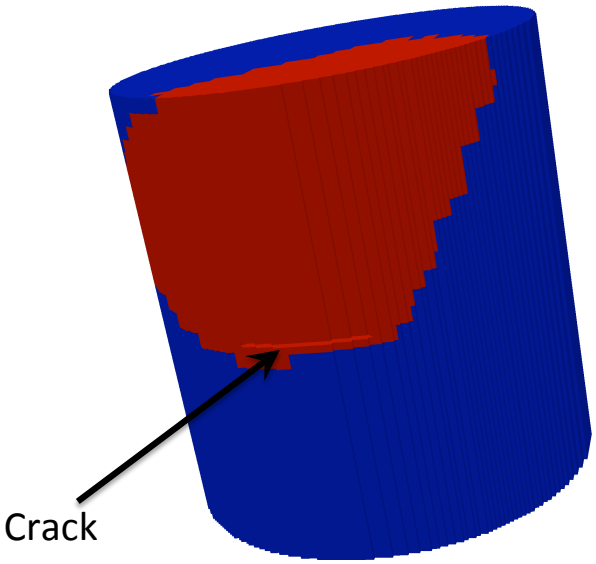


**Figure 3.3:** Shape and position of the reoriented grain, is to note that the smallest crack is completely embedded in it

# Chapter 4

# Results and discussion

## 4.1 Macroscopic variables

Distributions in microscopic features, such as microstructure and flaws within a material dictate the variability in macroscopic performance, ranging from yielding stress to low/high cycle fatigue life; Irwin [21] was the first to point out how fracture toughness depends upon plastic behavior ahead of the crack-tip; subsequently Rice and Thomson [44] proposed a model that could account for stress relaxation and crack blunting based on dislocations emission at the crack-tip. With the recent advent of molecular dynamics (MD), Abraham et al. [1] simulated the plastic behavior at the crack tip inline with the theory discussed by Irwin and Rice. Building from these simulations, Argon [4], Giannattasio and Roberts [17] investigates how the mobility of dislocations is responsible for crack growth and arrest while George and Michot [16], Gumbsch et al. [19] studied the relation between crack growth rate and dislocations multiplication at the crack-tip in Silicon single crystal. In Figure 4.1, the macroscopic response to uniaxial tensile test is depicted for both the experimental data used for the fitting procedure and the 7 different microstructure realization with a crack length of $a = 0.66 \quad \mu m$. As can be seen, the macroscopic behavior is not exactly equivalent through the different realizations; this

is due to the fact that the reoriented grain occupies a large volume inside the microstructure (see Figure 3.3). A difference of the aggregate in both the yielding stress and stiffness can be noted, although we note that this macroscopic behavior is not influencing our results mainly for 2 reasons: (a) the highest difference in uniaxial stress response of the different realizations at 3% strain is 50 $MPa$ (see Figure 3.3), which if compared with the absolute stress value at this strain is below the 5% engineering threshold; (b) we are interested in the variability at the crack-tip, where the stress and strain fields induced are dominant compared with this small deviation. By relating the uniaxial response to the IPF, we note that similar orientations have nearly the same macroscopic response, i.e. the pairs Random3 (green) and Random4 (gray) or Random2 (gold) and Random6 (purple). Despite this similarity, further investigation of the full stress field images reveals differences in local behavior, as shown in both Figures 4.2 and 4.3.

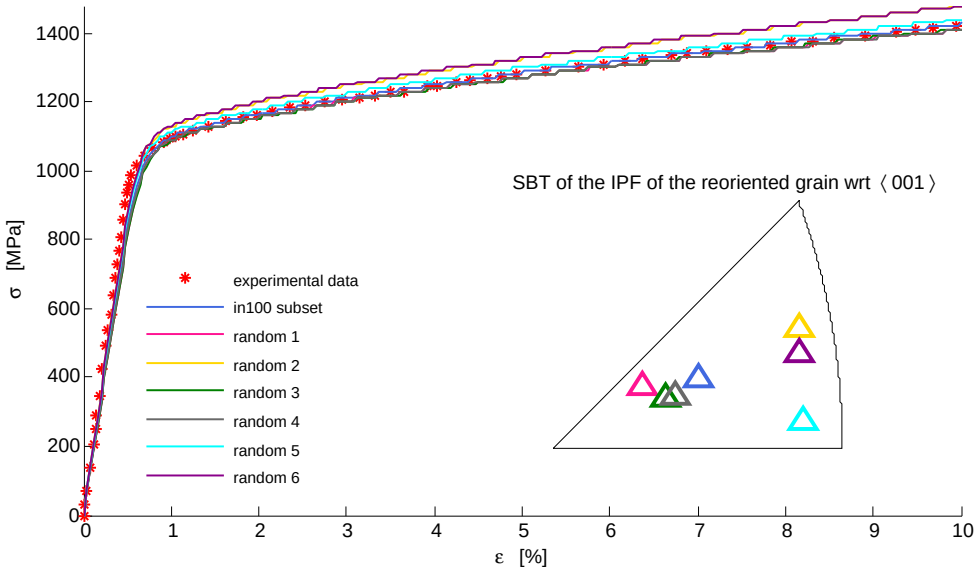


**Figure 4.1:** Macroscopic uniaxial tension ($\sigma_{33}$ vs $\varepsilon_{33}$) results of the 7 cracked microstructure realizations and experimental data used for fitting. The variability in macroscopic behavior change a lot with grain orientation, this is due to the fact that the reoriented grain occupies almost 17% of the entire microstructure.

Figures 4.2 and 4.3 show the equivalent Von Mises stress field of the 7

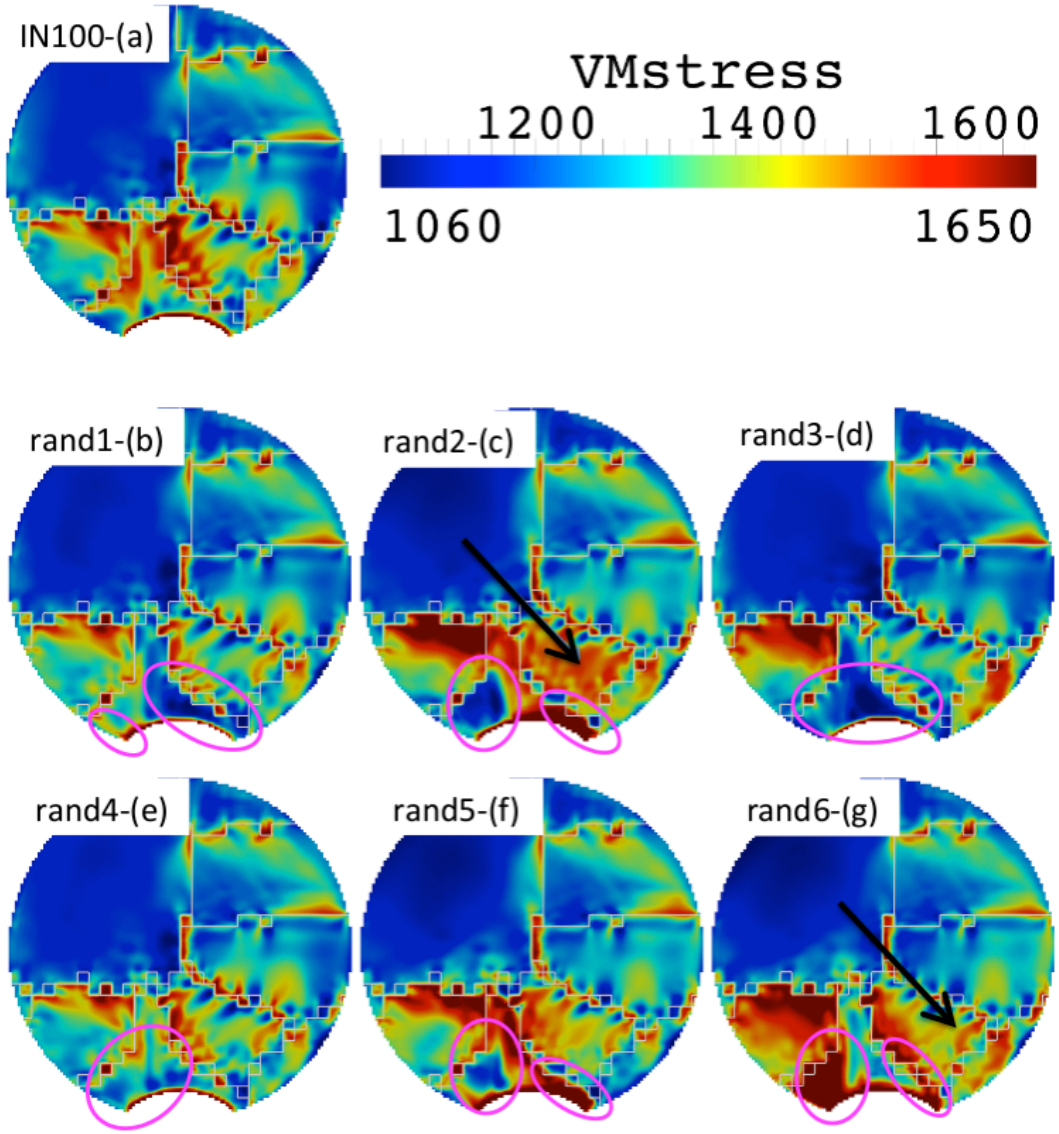


**Figure 4.2:** Comparison of deviatoric Von Mises equivalent stress field on the crack plane, for the 7 different microstructure realizations at 3% macroscopic strain : pink ellipse highlight zone with where the field difference is appreciable (e.g. hot spots). By varying the orientation of the cracked grain, the stress field is modified throughout the polycrystal and not only in the closes neighbor grains.

realizations on 2 different sections, the former refers to the plane perpendicular to the loading axis through the crack plane and the latter is normal to the crack plane through the symmetry axis of the ellipse, both at 3% global strain to emphasize the plastic behavior variability. The lowest value in the color-map corresponds to the macroscopic yielding value, $\sigma_y = 1060 \quad MPa$, and the pink

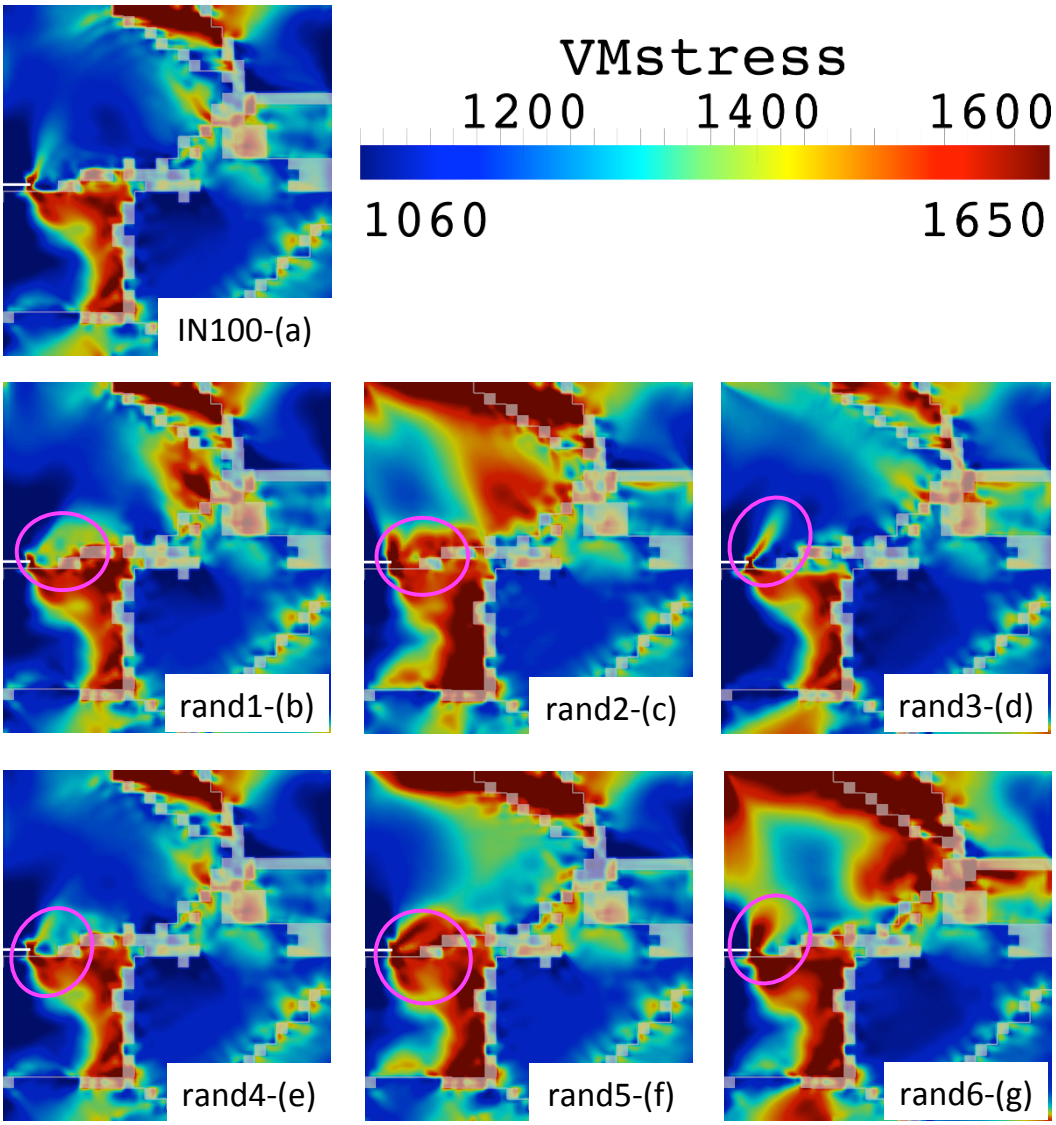


**Figure 4.3:** Similar to Figure 5, except that here we are looking at the plane normal to the to the crack plane.

ellipses denote some of the major differences between each of the 6 random realizations and the original one. Also, for brevity, we will name deep red zones, which identify highly stressed and plasticized areas, as hot spots and denote the deep blue areas, which identify low stress and non plasticized zones, as cold-spots. Very complex stress fields are found both in the proximity of the crack tip and near crystallographic flaws like GBs. The microstructural features like GBs represent stress concentrators that are not accounted for in classical linear elasto-plastic fracture mechanics (LEPFM). For this reason,

additional insight is needed to capture the complexities of the SCG behavior. These results are in agreement with the local multi-axial stress state generated by a uniaxial tension applied to a polycrystalline specimen, as pointed out by Guilhem et al. [18] on 2D simulations and to the non isotropic behavior of plastic zone outlined by Potirniche et al. [43] in their bi-crystal CP-FEM simulations. As previously noted, equivalent macroscopic behavior can lead to different local behavior analyzing the pair of realizations Random2 and Random6, depicted in Figures 4.2 (c) and (g), respectively, we can immediately recognize variability ahead of the crack tip in fact, the hot and cold spots show a complete opposite behavior in these 2 realizations despite their similar orientation (see Figure 4.1). In Figure 4.2(c), we can identify a cold spot on the left which is distinct from the GB and a hot spot on right which interacts with the GBs structure just in front of the crack-tip, extending until the first GB. In Figure 4.2(g) the hot spot is moved on the left side in the same position of the cold spot, while on the right side a smaller hot spot is found, creating a link between the stress induced by the crack-tip and GBs structure suggesting a possible crack path. Furthermore, this variability influences the distribution of the stress in the neighboring grain. By viewing two realizations, which share a similar position in the IPF, Random3 and Random4 depicted in Figs. 4.2 (d) and (e), respectively, we see despite the similarities in the cracked grain orientation and stress field plot, the average level of the von Mises stress ahead of the crack-tip shows a variability around 200 $MPa$. In both cases, the differences in the hot/cold spots extension and position suggests that the crack may grow at different rates in different directions due to the presence of the GBs Potirniche et al. [43] and misorientation between neighboring grains Ferrie and Sauzay [14]. Furthermore, the different behavior experienced by neighbor grain indicates the need to analyze clusters of grains as pointed out by Guilhem et al. [18], Sangid et al. [52] within a possible SCG theory. As first pointed out by McEvily and Boettner [29], dislocations are emitted in an orderly manner from the crack tip on highly stressed slip planes. By inspecting

the variability in Figure 4.3, we note the difference in the angles, extension, and shape of the lobes of hot spots surrounding the crack-tip and their wake. The difference in angle between the various realizations is a clear indication of the influence of grain orientation at the crack tip; the difference in size reveals the influence of grain orientation on the plastic zone and subsequently on fracture toughness and growth rate, while asymmetry of these zones contains information about neighboring grain misorientation and distance. The first thing that should be noted is that a GB is present just beneath the crack, leading to high stresses in this direction. Moreover not all the realizations show the same hot spots features in this area, for instance: Random3 and Random5 depicted in Figs. 4.3 (d) and (f), respectively, have a branch of the hot spot following the GB direction; while Random6 depicted in Figure 4.3(g) has a very bulky hot spots following the GB and extending very deeply in the neighbor grain; further, in other realizations, such as IN100, Random1, and Random4 in Figs. 4.3 (a), (b) and (e), respectively, we can observe that the hot spot below the crack-tip, after passing through the GB, follows a well defined orientation imposed by the slip plane of the neighboring grain. By viewing the hot spots in the cracked grain, we observe the IN100 and Random4 realizations (see Figure 4.3 (a) and (e), respectively) show a very limited hot spot at the crack-tip with a big plastic zone at a lower stress level, Random3 (see Figure 4.3 (d)) has a long hot spot with a well defined direction and a very tight wake, Random6 (see Fig 4.3. (g)) shares the same well defined behavior of Random3 but with a much thicker hot spots and wake areas. Random3 has hot spots oriented almost in the load direction, with a hot spot bridging towards the highly stress zone at the crack tip, with the one at the GB. Random5 has 3 hot spots departing from the crack-tip in 3 well-defined direction. Additionally, we note that images obtained at lower strains show that plasticity starts to play a role as the global behavior is in the linear elastic zone and that the shape of plasticized areas at lower strains are consistent with the ones shown in Figures 4.2 and 4.3. Furthermore in some cases, hot spots

are found not at the crack tip, but in its vicinity just passed the GB displaying the effects of stress anisotropy between grains. We can briefly explain this behavior from a dislocations dynamics point of view. Smaller hot spots areas in both Figures 4.2 and 4.3 indicate emission of edge dislocations at the crack-tip on highly stressed slip planes, which have the property to relax stresses by blunting the crack and in turn diminishing the avalanche mechanics of dislocation emission, ¸itebitzek In general, the hot spots and preferred sites for dislocation emission could be in place only on a portion of the crack-tip surface, thus explaining differences in behavior amongst the different spatial locations and realizations enhancing variability. GBs act as both dislocation sources and energy barriers to incoming dislocation Sangid et al. [51], creating local hot spots ahead of the crack-tip in the bulk of the material. A bridging effect between hot spots is observed between the GBs to the crack-tip and vice versa. This phenomenon does not always follow the primary hot spots orientation suggesting that more than one slip plane has been activated, e.g. Figure 4.3(c). Furthermore, according to Lee et al. [28], the interaction between dislocation and GBs can have 3 major consequences: (i) cross-slip into adjacent grain, (ii) partial transmission, resulting in residual dislocation incorporated in the grain boundary, (iii) dislocation blocked at the GB; eventually mechanisms (ii) and (iii) can lead to impeded dislocation motions Sangid et al. [52] and subsequently preventing further dislocation emission.

## 4.2 Slip system activity

As can be seen from Equation 1.18, the plastic flow is governed by the resolved shear stress, which is linked to the stress tensor by the well-known relation

$$\tau^{\alpha} = \frac{1}{2}\sigma : (\hat{n} \otimes \hat{m} + \hat{n} \otimes \hat{m}) \tag{4.1}$$

where $n^{\alpha}$ is the normal of the slip plane and $m^{\alpha}$ is the slip direction. To achieve a better insight of variability at the crack-tip, a statistical analysis of the resolved shear stress has been performed on the crack plane. Figure 4.4(a) shows the probability density function of the active slip systems of the 7 different realizations with a crack length $a = 0.66 \quad \mu m$ at 3% strain over the volume schematically represented by grey dots (as shown in the inset within Figure 4.4(a), where each dot represents a voxel.

The dash-dotted vertical lines represent the maximum and the minimum value of the averaged resolved shear stress at the crack-tip (represented by black stars in the schematic), while dashed vertical lines represent the same quantity 4 voxels ahead of the crack-tip (represented by red stars). Figure 4.4(b) depicts the cumulative density function. The first thing that should be noted in Figure 4.4(a) is that the curves are not equal area, as can be clearly seen in Figure 4.4(b), meaning that a different number of slip systems are activated in different realizations. Recently Zhang and Ghosh [65] investigated the relationship between grain orientation and dislocations emission on a pre-cracked Nickel single crystal through MD simulations, they found a variability in both type and number of dislocations depending on the orientation, which subsequently interact with each-other in different ways leading to completely different material performance. This same behavior is observed in our simulations at the scale of the microstructure. Furthermore many other parameters underlying the variability in material behavior at the crack-tip can be noted. The resolved shear stress range at which peaks are found, is consistent with the position of the average resolved shear stress 4 voxels ahead of the crack-tip, in other words, moving away from the crack-tip the average value of the resolved shear stress is less sensitive to crack influence becoming more homogenous, i.e. a range of 655.2 MPa maximum spatial average of the RSS observed in Random6 compared to a value of 530.8 MPa, which is the minimum spatial average of the RSS observed in Random2. Also, the volume fraction at which peaks are found undergoes a high variability, going from 6% of Random4 to more

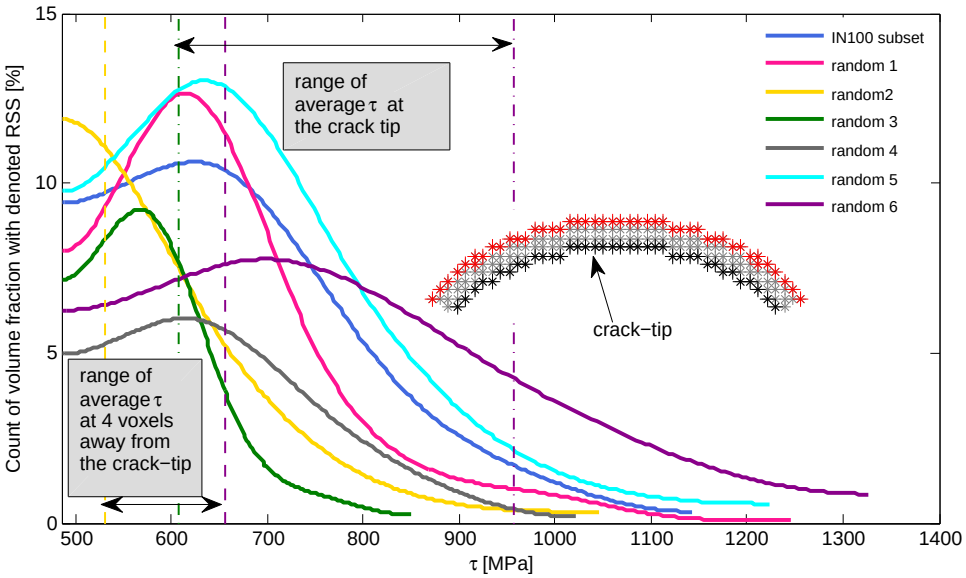


(a) Probability density function of the active slip systems versus resolved shear stress in the first 4 rows of voxels in front of the crack tip, whitin the crack plane (see figure). It should be noted that this curves are not equal area and start from critical resolved shear stress. In the case when the macroscopic results are almost the same (i.e. random2 and random6 realizations), their distributions and peak positions vary significantly

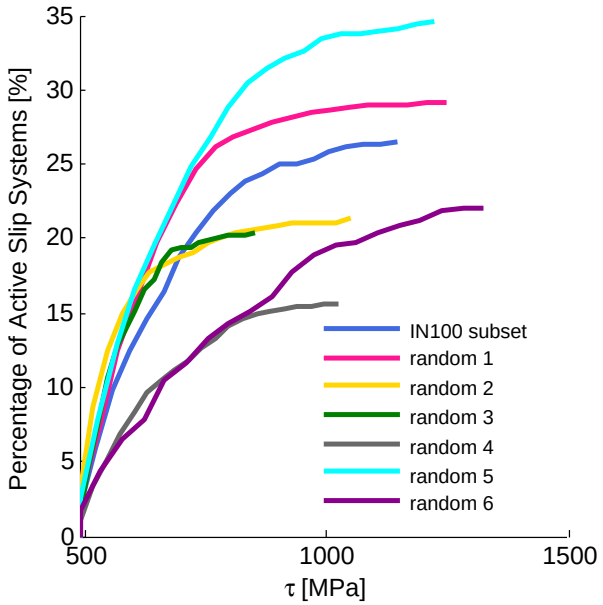


(b) Cumulative density function: the figure shows that a very different slip activity is present in front of the crack-tip within the crack plane, and that the number of active slip system is not only related to the orientation of the cracked grain: i.e. random 3 and random 4 realizations, that are really close in the IPF figure, has a substantial difference in the count of active slip systems

**Figure 4.4:** Slip System Activity at the crack-tip

13% of Random5 realizations. By changing the analyzed volume and moving at the crack tip, more variability is seen in the averaged resolved shear stress, e.g. more than 300 $MPa$, which depicts a complex scenario that cannot be resolved by simply viewing the grain orientation or SchmidÕs factor. Analyzing comparable IPF realizations (see Figure 3.3) like the pair Random3 and Random4, the variability in behavior is evident by viewing their tail length, peak position and volume fraction. A similar variability can be seen in pairs of similar orientations of the cracked grain, Random2 and Random6, by looking at the average value of the resolved shear stress 4 voxel away from the crack tip, of which these realizations represent the 2 extreme values. The result of which emphasizes the need to account for this variability in slip activity as this has direct implications on the crack driving force. The variability observed in the tail length of the strain rate probability density function are related to strain localization (Moulinec and Suquet [36], Rollett et al. [47]), which is pertinent to identify favorable slip planes for crack growth as pointed out by McEvily and Boettner [29]. From a SCG point of view, variability needs to be addressed, and as we move closer to the crack-tip, the its effect becomes more and more dominant (as shown, see zones of average of resolved shear stress in Figure 4.4(a)); due to crystallographic features and flaws that play a crucial role in dislocations emission and evolution, which in turn influence growth rate. It should also be noted that these finding, especially the total percentage of active slip systems suggest localized activity in highly stressed slip planes, that can lead to localized damage. In their work Sadananda and Glinka [50], pointed out the direct dependence of SCG advancement from dislocation emission at the crack-tip, and how the interaction between dislocations, microstructure and flaws can lead to very complex dislocations arrangement due to different mechanism like activation of different slip system, cutting of dislocations, annihilation of edge dislocations producing vacancies, cross-slip of screw dislocations, shearing particles, presence of GBs, etc. All these mechanisms can lead to slip irreversibility, which are proportional to the SCG rate

(Mughrabi [37]). The complex scenario shown in this section elucidates the critical role of slip-irreversibility that is directly influenced by variability in the microstructure, due to different slip-system activity, leading to different cyclic damage accumulation, which in turn will lead to variable SCG rate, influencing macroscopic performance.

## 4.3 Damage quantification

At this point, it is pertinent to quantify damage accumulation. As stated by Mughrabi [37], damage accumulation can occur in both surface and bulk of fatigued metals. Recently the research community has used different fatigue indicator parameters (FIPs) to quantify damage accumulation, for instance Hochhalter et al. [20] in their work define 5 different FIPs, of which 3 based on accumulated plastic resolved shear-strain, 1 based on maximum energy dissipation, and the last one based on the Fatemi-Socie parameter. The work of Fatemi and Socie [13] focused on multi-axial fatigue and emphasized the role of normal tensile stress on the critical plane, following the work of Brown and Miller [10]. The importance of the critical plane in multi-axial fatigue has been emphasized on the slip plane scale, which has been investigated also by Bennett and McDowell [6] and recently confirmed Tschopp and McDowell [61] using MD simulations to show that a normal stress on the slip plane considerably lowers the shear stress required to nucleate a dislocation loop. In our work, we will use 3 of the 5 FIPs analyzed by Hochhalter et al. [20] and we will maintain the same nomenclature for coherence:

$$D1 = \max_{\alpha} |\Gamma^{\alpha}| \tag{4.2}$$

$$D3 = \sum_{\alpha=1}^{N} |\Gamma^{\alpha}| \tag{4.3}$$

$$D5 = \max_{p} \sum_{\alpha=1}^{N_s} |\Gamma_p^{\alpha}| \left(1 + k\frac{\langle \sigma_n^p \rangle}{\tau_0}\right) \tag{4.4}$$

where $\Gamma^{\alpha}$ is the accumulated plastic resolved shear-strain on the selected slip system, $N$ is the total number of slip systems, $p$ identify the slip plane, $\langle \sigma_n^p \rangle$ is the tensile stress acting on the slip plane $p$ ($\langle \bullet \rangle$ are the Macaulay brackets defined such that $\langle x \rangle = 0$ if $x \leq 0$ and $\langle x \rangle$if $x > 0$), $k$ is the weighting factor dictating the importance of tensile stress with respect to plastic slip, that has been set to 0.5 as suggested by (Fatemi and Socie, 1988), and $N_s$ is the number of slip-system on each plane. Physically Equation 4.2 represents the slip system with the maximum accumulated plastic resolved shear-strain, Eq. Equation 4.3 represents the total accumulated plastic resolved shear-strain in each voxel, while Equation 4.4 represents the maximum accumulated plastic shear-strain amongst planes subjected to tensile normal stresses. It should be noted that in literature these FIPs have been used to quantify the slip irreversibility at the end of a fatigue cycle. Within our EVP-FFT framework, we limit our analysis to monotonic loading, thereby limiting our possible sources of slip irreversibility but still identifying hotspots in the microstructure as potential sites for slip irreversibilites. Additionally, we investigated 3 FIPs based on energy dissipation that have been formulated as follows (Korsunsky et al. [23]):

$$E1 = \max_{\alpha} |\Gamma^{\alpha} \tau^{\alpha}| \tag{4.5}$$

$$E3 = \sum_{\alpha=1}^{N} |\Gamma^{\alpha} \tau^{\alpha}| \tag{4.6}$$

$$E5 = \max_{p} \sum_{\alpha=1}^{N_s} |\Gamma_p^{\alpha} \tau_p^{\alpha}| \left(1 + k \frac{\langle \sigma_n^p \rangle}{\tau_0}\right) \tag{4.7}$$

which are the energetic equivalent of D1, D3, D5. Figures 4.5(a) and 4.5(b) display the reference systems of: $\theta$, the angle of maximum FIPs direction on the plane normal to the crack and $\varphi$, the angle of maximum FIPs position at the crack tip. This reference configuration with the angles of maximum FIP directions, $\theta$ and $\varphi$, will be used throughout the discussion.

In Figure 4.6, the contour plots of all 6 different FIPs, Equations from 4.2 to

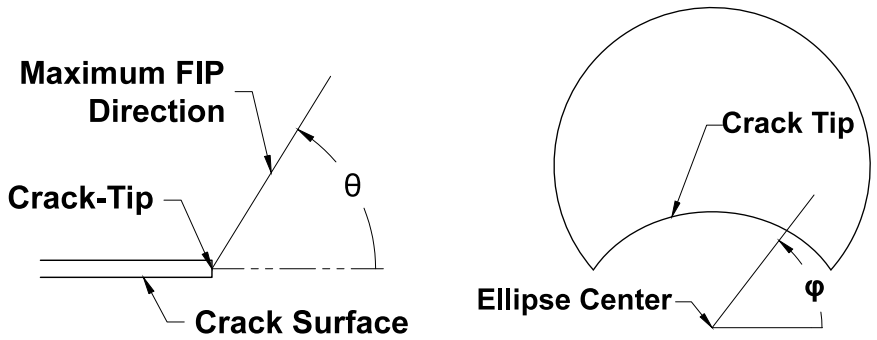


(a) schematic of maximum FIP angle reference system in plane normal to the crack

(b) schematic of maximum FIP angle reference system in the crack plane

**Figure 4.5:** Maximum FIP directions

4.7, are depicted, at a macroscopic strain $\varepsilon_{33} = 0.32\%$. It should be noted that at this strain level, the direction of maximum FIP, namely $\theta$, is around $\pm 90°$, this is due to the fact that plasticity is still not well developed (see Figure 3.3). Additionally, while FIPs D1, D3, D5, which are based only on plastic strain, have a very similar behavior and shape, as pointed out by Hochhalter et al. [20]; E1, E3, E5 are much more sensitive to crystallographic features, which can be seen in Figures 4.6 (d), (e) and (f). The shear-based FIPs show their maximum at a spatial location a voxel behind the crack-tip, due to the increase compliance at the crack flanks coupled with the stress concentration near the crack tip, although this depicts a non-accurate scenario for damage accumulation due to low plasticity level. While we note the energetic FIPs, E1, E3, and E5, display their maximum at the crack tip, which is the traditional location for maximum damage; thereby emphasizing their importance to the fatigue process. The complete FIPs evolution for the IN100 realization is shown in Video A.1, which is available as a supplement to this work. Due to this reason, E5 is taken as the most complete FIP, thus it is used exclusively in the contour plots for the rest of this section. Figure 10 shows the contours plot for the 7 different realizations with a crack length $a = 0.66 \quad \mu m$ at a strain $\varepsilon_{33} = 3\%$.

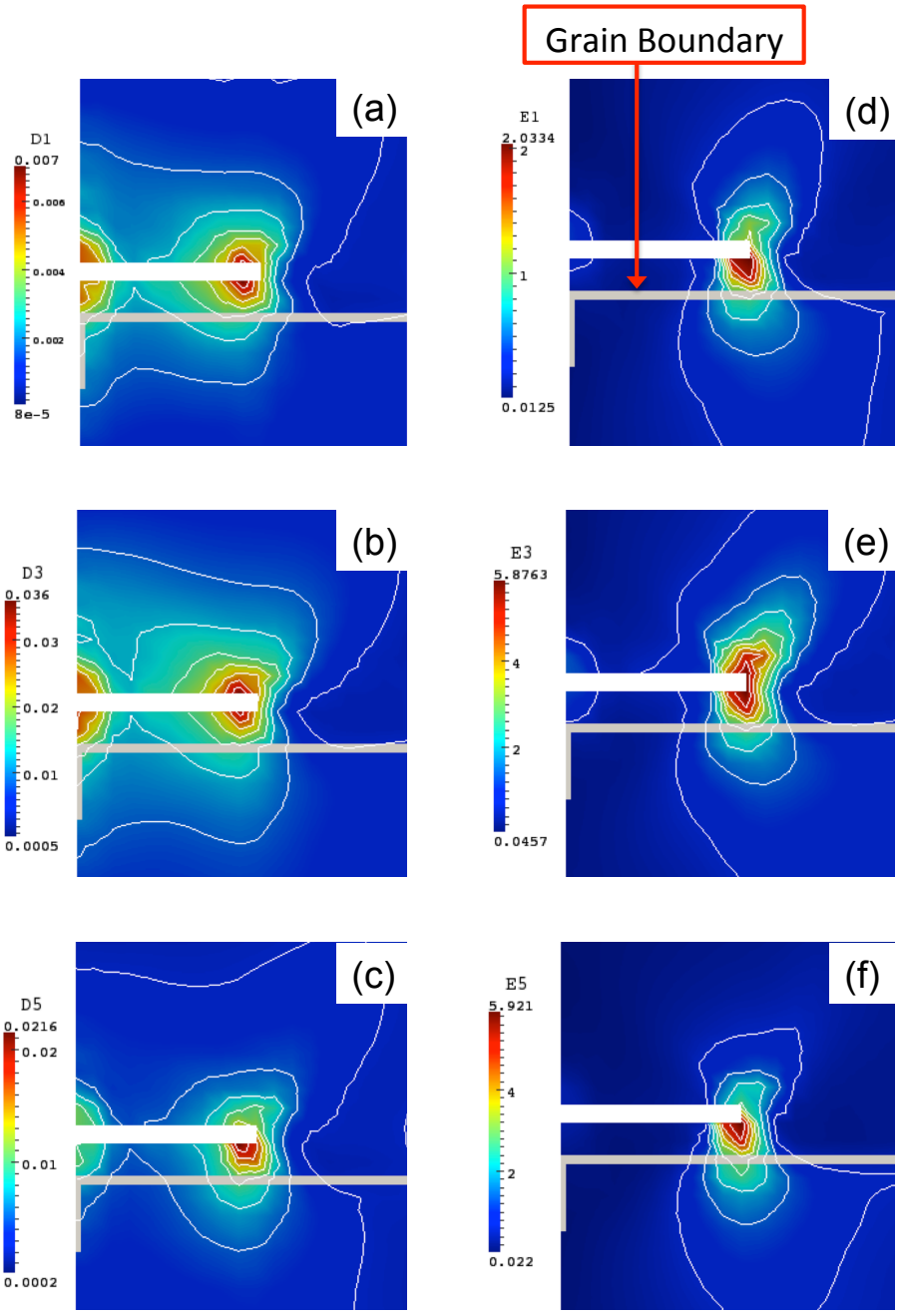


**Figure 4.6:** Different FIPs field comparison at the crack tip of the IN100 subset, at low strain $\varepsilon_{33} = 0.32\%$ (almost in the middle of the linear elastic region as shown in Figure 4). It should be noted that at this strain, the direction of maximum FIP is around $\pm 90°$ this is due to the fact that, at this strain, plasticity is not well developed. Furthermore it should be noted that even at low strain the shape of this 6 indicators are very different, also the 3 energetic indicators seems to be more sensitive microstructure features like Grain Boundaries

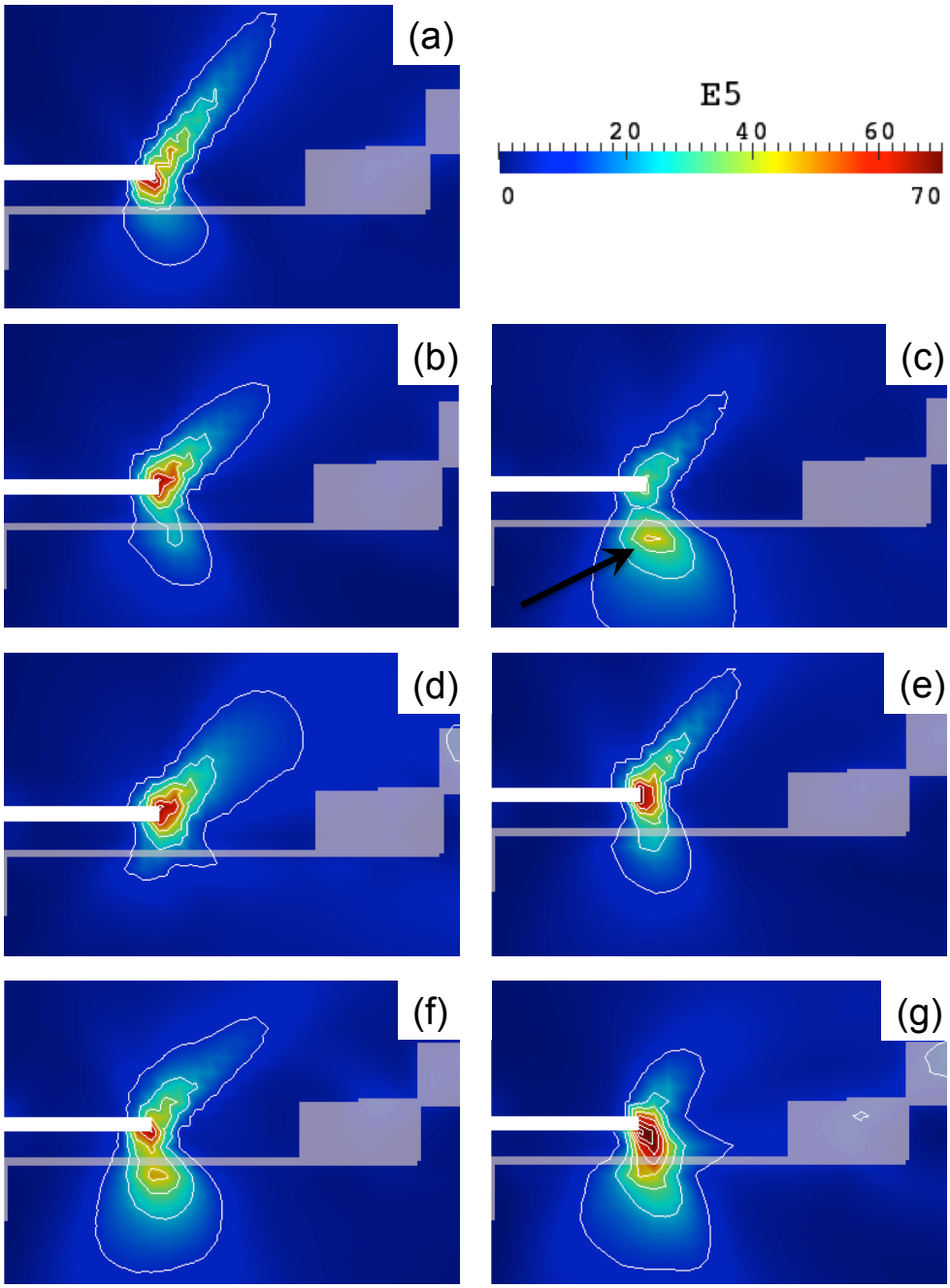


**Figure 4.7:** Different FIPs field comparison at the crack tip of the IN100 subset, at low strain $\varepsilon_{33} = 0.32\%$ (almost in the middle of the linear elastic region as shown in Figure 4). It should be noted that at this strain, the direction of maximum FIP is around $\pm 90°$ this is due to the fact that, at this strain, plasticity is not well developed. Furthermore it should be noted that even at low strain the shape of this 6 indicators are very different, also the 3 energetic indicators seems to be more sensitive microstructure features like Grain Boundaries

The first thing that should be noted is the variability in maximum value of the E5 FIP between the different realizations. For instance Random6, which is depicted in Figure 4.7 (g), shows the widest hot-spot area, in contrast to Random2 (see Figure 4.7 (c)), which has the minimum value. Furthermore, the variability can be noted in the location of the hot spot with respect to the crack tip, e.g. the former is located near the crack tip, while the latter denotes subsurface damage (see black arrow in Figure 4.7 (c)). These differences are notable, yet these distinct microstructure realizations (Random2 and Random6) have similar orientations of the cracked grain as denoted by their position in the IPF (see Figure 3.3). By viewing another pair of similar orientations of the cracked grain (Random3 and Random4 in Figs. 4.7 (d) and (e)), the former shows grain shielding with a positive angle $\theta$, while the latter shows nearly a symmetric profile, e.g. 2 lobes in 2 different directions almost of the same intensity. The damage accumulation can be correlated with different physical phenomena, for instance as the crack-tip is proximal to a GB, we can observe sudden change in crack-direction (Hochhalter et al. [20]). This is attributed to the irreversibility of slip near the GB. When a dislocation impinges upon a GB, in most cases due to strain incompatibility, a residual dislocation is formed within the GB, which is often a form of irreversibility in fatigue (Sangid et al. [51]). As damage in the form of slip accumulates at the GB and the GB is saturated with dislocation content, the crack can propagate in the direction of the GB leading to intergranular cracking or continue along slip planes resulting in transgranular cracking. Grain shielding is an effect due to GBs that impede dislocation motion or dislocation entanglement between the crack-tip and the GB. In the first case dislocation will follow the minimum energy principle for propagation, propagating inside the grain where slip resistance is lower, this could be achieved with a high misorientation between all the slip planes in the adjacent grains, while the second option is due to a dislocation pile-up at the GB that in turn will generate a high stress field impeding dislocation propagation in this direction. As shown in Fig. 10, many

of the contour plots of the E5 FIPs traverse the GB, which is below the crack. In these cases, slip transmits past the GB, which is typically a low angle GB (defined by misorientation angle (see Equation 1.37) between the neighbor grains less than 15°). For a better understating of the E5 FIP evolution with various microstructure realizations, we invite the reader to watch Video A.2 as an Appendix. Figure 4.8 shows the 3D iso-surfaces of $E5 = 25 \quad Jm^{-3}$ of 4 different realizations, namely (IN100, Random2, Random3 and Random5) at global strain $\varepsilon_{33} = 0.76\%$ with a crack length $a = 0.66 \quad \mu m$. We would like

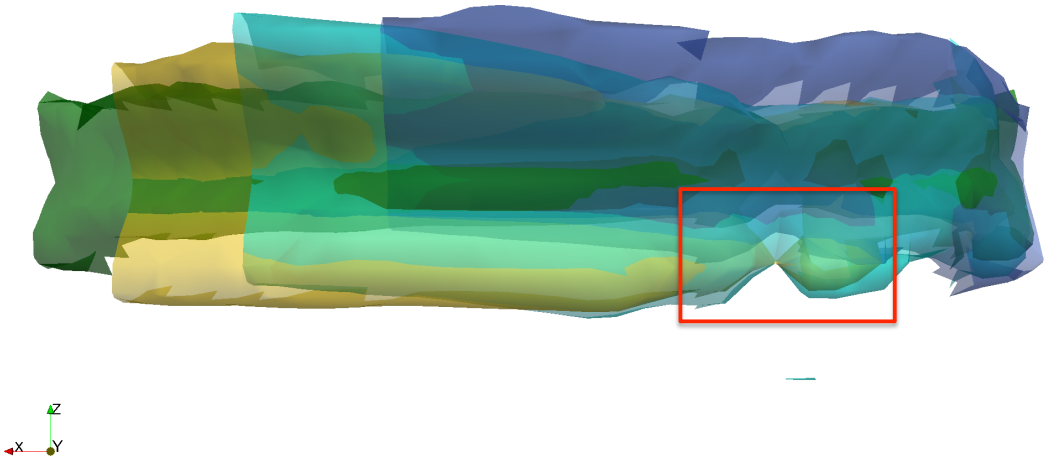


**Figure 4.8:** Iso-surfaces at the crack tip of FIP E5, colors are coherent with IPF. It should be noted the differences in shape and size, while some microstructure features are in common i.e. hot/cold spots for some realizations (see highlighted zone in the figure).

to point out the different shapes and features of these surface that highlight the variability of the depicted realizations (the colors indicated are coherent with IPF, see Figure 3.3). The microstructure realization denoted Random3 has the smallest surface indicating less damage accumulation, except in the central area ahead of the crack tip. The IN100 realization displays a constant height of the FIP iso-surface ahead of the crack tip, while the others gradually taper off. We invite the reader to visualize the evolution of these iso-surfaces in Video A.3 in the online Appendix. Figure 4.9 shows the quasi-static crack growth process depicting different contour plots for the IN100 realizations at different crack length at $\varepsilon_{33} = 3\%$. As expected, the maximum value of E5 is

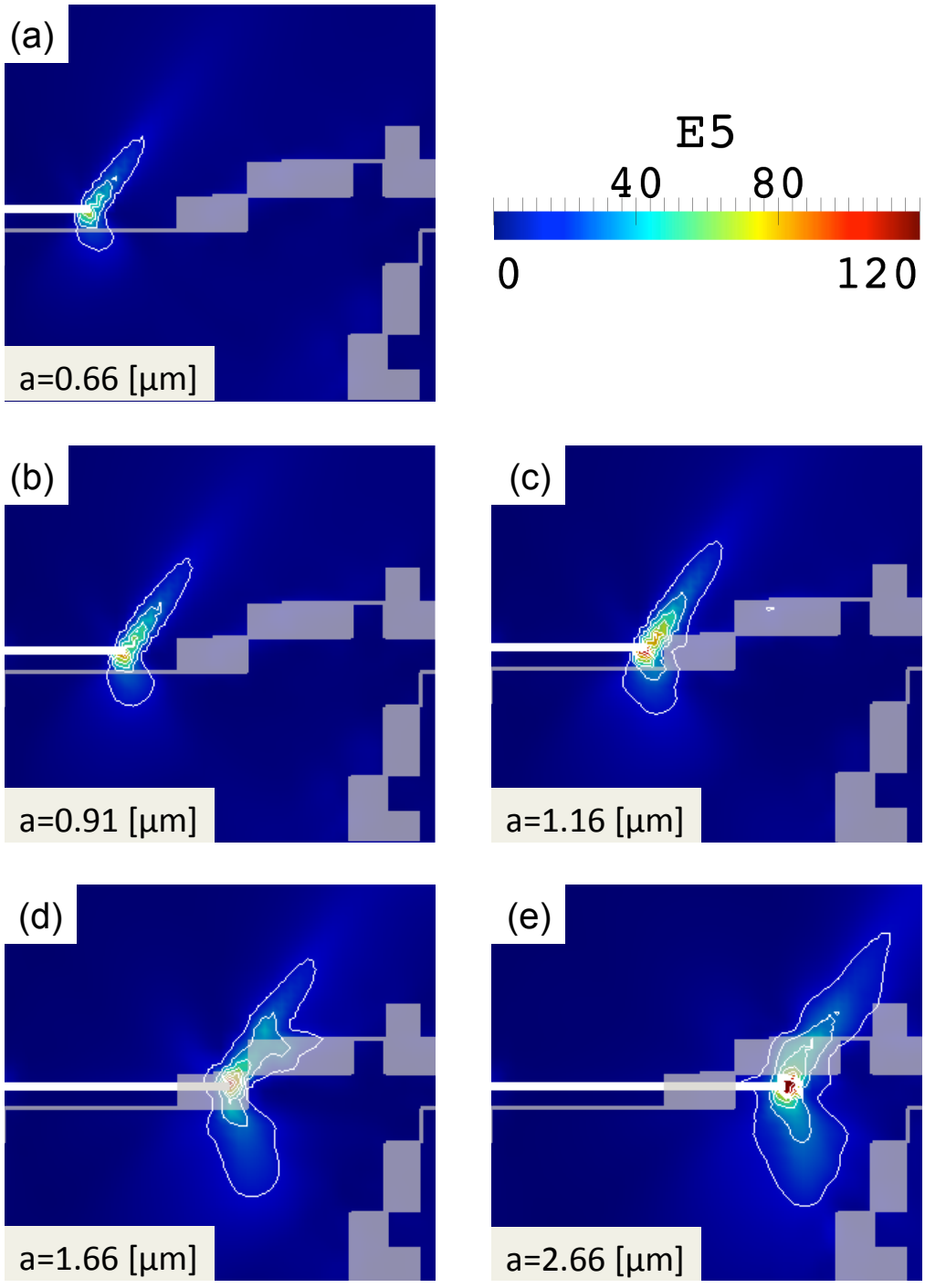


**Figure 4.9:** Comparison of E5 in IN100 subset at different crack lengths. In this figure, by increasing the crack lengths, as the crack moves towards more complex microscopic features, i.e. grain boundaries, the shapes of the FIP iso-surfaces change very significantly. At $a = 1.66$ $[\mu m]$ we can see how the iso-surfaces is following the GBs away from the crack tip; compared with $a = 2.66$ $[\mu m]$, the iso-surfaces seem to through GBs almost without being affected.

increasing with increasing crack length, as shown by the increasing area of the damage region and the contours within the region. The shape of the damaged region is not distinctively different until the crack reaches the microstructure, namely until $a = 1.16 \quad \mu m$. A more complex behavior of the damaged zone is depicted in Figure 4.9 (d) and (e), as the stress fields associated with the crack interact with the elevated stress fields due to the features (GBs) in the microstructure. As can be seen in Figure 4.9 (d), the damaged zone branches or bifurcates in the direction of the GB. It should be noted, that the range of the E5 FIPs undergo substantial variability in their value with respect to the length of the crack, more than 2 orders of magnitude. We invite the reader to watch Video A.4 as an Appendix. In order to consolidate the results of the quasi-static crack growth for the 7 microstructure realizations at different strain levels, we pick a representative candidate as depicted in Figure 4.10.

Figure 4.10 (a) shows the location of the maximum FIPs (D1, D3, D5, E1, E3, and E5) on the crack tip, in this case, the location of max FIP coalesce at the same position, but in general the maximum FIP value does not occur. Figure 4.10 (b) indicates the values of the nondimensionalized FIPs vs. distance from the crack-tip along $\varphi$ (see Figure 4.5(b) for orientation. In Figure 4.10 (c), it can be seen that the direction of maximum FIPs do not coalesce on the same direction and except for seldom cases, they are not in alignment with the slip planes in the microstructure. Finally, Figure 4.10 (d) displays the maximum value of the nondimensionalized FIP along angle, $\theta$ (see Figure 4.5(a)). As discussed by many authors in the fatigue literature, such as McEvily and Boettner [29], Brown and Miller [10], Fatemi and Socie [13] , and Bennett and McDowell [6] for example, the critical plane plays a significant role within fatigue phenomenon. In order to elucidate the role of the critical plane, we analyzed the alignment of spatial path of maximum FIP value with the slip planes in the microstructure and principal stress axes during loading.

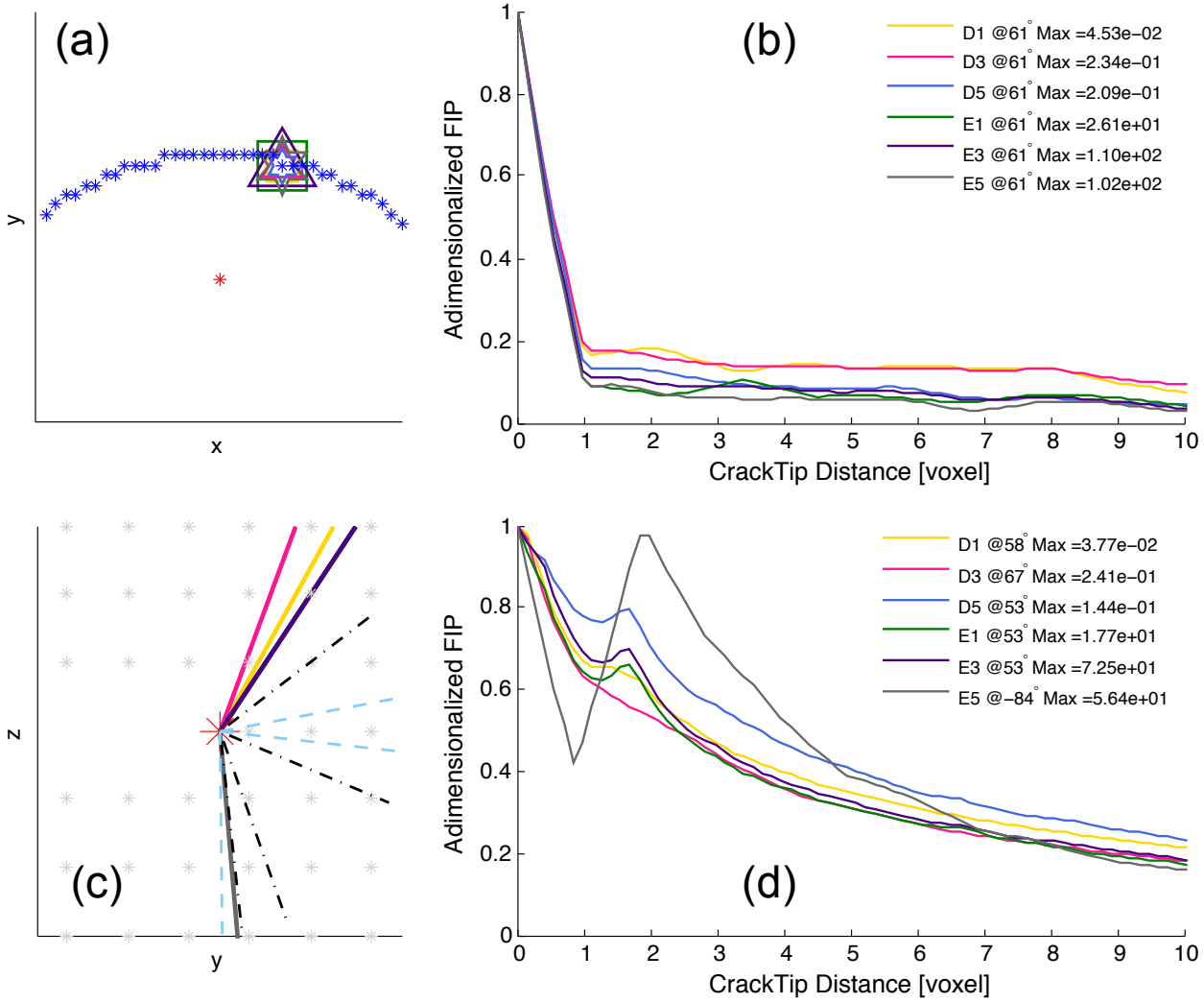


**Figure 4.10:** This particular case represents the subsurface damage (see Figure 4.7 realization random 5 ). (a) The spatial line relatively to the crack plane in which the FIP has been evaluated, blue dots represent the crack tip, red dot, the center of the ellipse, and symbols on the crack tip, the location of the maximum FIP at the crack-tip. (b) The values of nondimensionalized FIP with respect of its maximum vs. crack tip distance, in this case their values drop very rapidly going away from the tip in the crack plane. (c) The spatial line relative to the normal (cross-section) of the crack plane indicating the maximum FIP angle, black dashed line represent the projection of the 4 slip planes in the middle section of the ellipse, normal to the crack plane, and blue lines represent principal stress axis. It can be seen how some FIPs are aligned with slip planes like E5 in this particular case. (d) Along the spatial line in (c) the value of the each FIP is plotted along its maximum direction. The maximum value as not always located at the crack-tip, but can be ahead of the crack.

Figure 14 (a) depicts the average misalignment, given by,

$$\overline{\Delta\theta}_i = \frac{\sum_{q=1}^{Nsim} \Delta\theta_i^q}{Nsim} \tag{4.8}$$

where $Nsim$ is the number of different realizations (7), i identify the FIP and $\Delta\theta$ is the minimum absolute value of misalignment between the FIP maximum direction angle and the adjacent slip-plane/principal stress axis, at different strain level. Figure 4.11(b) shows the trend lines of (a) with error bars representing FIPs variability, and dots representing the average misalignment of all FIPs

$$\overline{\overline{\Delta\theta}} = \frac{\sum_{i=1}^{Nfip} \overline{\Delta\theta}_i}{Nfip} \tag{4.9}$$

where $Nfip$ is the number of different FIPs investigated (6), at each strain level. It should be noted that the misalignment between the slip planes and FIPs decreases, while the misalignment with principal stress axis increases.

This behavior is due to the fact that at small strains, plasticity has just started to develop and unevenly distributed damage starts to appear in the proximity of the crack-tip, while the majority of the material is still in the elastic regime, which is governed by principal stress axes. This behavior is typified by our choice of E5 as the most pertinent FIP. Additionally, the alignment of the FIP and slip planes with increasing strain is due to two different mechanisms: (i) grain rotation near the crack tip, in fact due to our very low strain rate, this can be a partial explanation; (ii) additionally, as pointed out by Bitzek and Gumbsch [7] in their recent MD work, previously stated by George and Michot [16], and confirmed by X-ray tomography results (Michot [32], Scandian et al. [54]), the more commonly observed dislocation source in crack propagation is a consequence of emission of multiple Burgers vectors on different glide planes at once, in other words multi slip plane activity, which explains the misalignment between FIPs and slip planes.

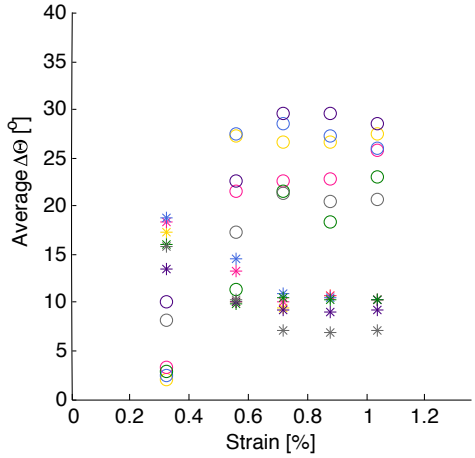


(a) Alignment between the spatial line trace of the maximum FIP to that of the slip planes (indicated by stars) and principal stresses axes (indicated by circles), as function of the macroscopic strain for a fixed crack length $a = 0.91$ $\mu m$

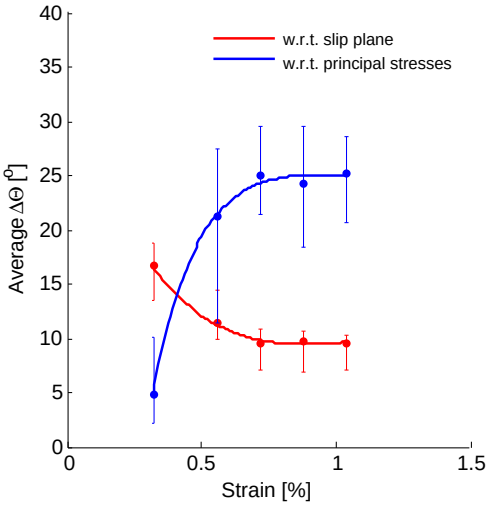


(b) Trend of diminishing distance between FIP and slip plane, and increasing between FIP and principal stress axes is shown, where error bar represents the minimum and maximum variation.

**Figure 4.11:** Average FIPs alignment at different strain level

## 4.4 Relationship with short crack growth

During the last decade, the demarcation of FIPs have emerged within computational materials modeling as a metric for the driving force for both crack

propagation and nucleation, i.e. Castelluccio and McDowell [11] found a 1 to 1 relationship between the Fatemi-Socie parameter and crack-tip displacement, Hochhalter et al. [20] investigated different FIPs for crack initiation and also hypothesized the use of FIPs for a linear prediction of damage accumulation, and Guilhem et al. [18] also investigated different FIPs for crack nucleation. In the well-known Paris plot of fatigue crack growth, e.g. the $da/dN$ vs. $\Delta K$ chart, the region 1 is typically denoted for short crack growth. In this region, the size of the crack is smaller than the prominent features in the microstructure. Hence, the plastic zone size ahead of the crack tip has strong interactions with the strain fields produced by the defects in the microstructure. For this reason, the region 1 short crack growth is strongly influenced by the microstructure. Albeit, there is not a theory in place to predict fatigue crack growth based upon the local microstructure, especially since stress intensity factors only have a dependence on the crack length, applied stress, and geometry of the crack, but none of these parameters account for microstructure. Further, since most engineering alloys experience a distribution of local microstructures, we expect variability in the short fatigue crack behavior. This is experienced by the variability in threshold measurements (Taylor and Knott [59]). For these reasons, it is important to quantify the variations in the FIP near the crack tip in the presence of variability in the microstructure. McEvily and Boettner [29] found that SCG rate in a single-crystal is an orientation dependent process. The grain orientations leading to higher degrees of work hardening are associated to high growth rate, while, in polycrystalline materials, crack advancement is a selective process based on favorably oriented grains. Yoder et al. [64] investigated the relationship between average grain size and the value of $\Delta K_{th}$ showing how it increases proportionally to the square root of the average grain size. Wilkinson [63] showed the dependence between SCG rate and the location of the crack tip, and how the distance between the tip and the boundaries influences the SCG rate. When the tip is in the core of the grain, the SCG rate is almost constant with a slight tendency to increase; compared to the case of

when the crack-tip approaches the grain boundary, it can increase or decrease, depending on the misorientation with neighboring grain. These microstructure variability parameters will influence slip character, strain accumulation, irreversibility and therefore growth rate modifying the $\Delta K_{th}$ value: (i) the cracked grain orientation influences the resolved shear stress on slip-systems, introducing variability in both strain accumulation and slip character. Thus leading to changes in the shapes and surfaces of the plastic zone ahead of the crack-tip within the cracked grain, and eventually in its neighbors, thereby modifying the threshold value for crack propagation; (ii) grain size define the density of GBs, introducing different mean free path lengths for dislocations motion that in turn will affect the stress-field around the crack tip, and eventually could prevent further dislocation emission (Sangid et al. [53]) strengthening the material and diminishing the SCG rate; (iii) the distance between GBs and crack-tip is another crucial parameter, in fact as the crack-tip approaches GBs, the interaction between the stress field induced by neighbor grains misorientation and the one generated by the crack-tip will affect slip transfer and in turn irreversibility. From a crystal plasticity perspective, the influence of all the parameters discussed in the previous paragraph can be taken into account, keeping track of slip-accumulation and resolved shear stress voxel by voxel. For these reasons the use of FIPs ( Equations 4.2 to 4.7) is a good choice to account for variability in $\Delta K_{th}$ value. Moreover, the original FIP, the Fatemi-Socie parameter, was constructed in a format analogous to a stress intensity factor, $\Delta K$ (Socie [57]). For this reason, we plot the nondimensionalized FIPs compared with crack size in the simulation as a likeness to compare against the Paris diagram. SCG shows a lower stress intensity factor threshold that is related with damage accumulation. We investigated the shape of all FIPs at different crack length. Figure 4.12 depicts the crack length vs. log of nondimensionalized FIPs at different strain level for all the realizations. It should be noted by decreasing the crack length, the variability increases, and vice versa. This behavior is typified in FIPs based on critical plane damage

accumulation, namely D5 and E5, which allows identification of the transition between microstructural short cracks (dependent on the microstructure) and macroscopically short crack (less sensitive to microstructure variability). The shape of the analogous nondimensional FIP vs crack length is similar to

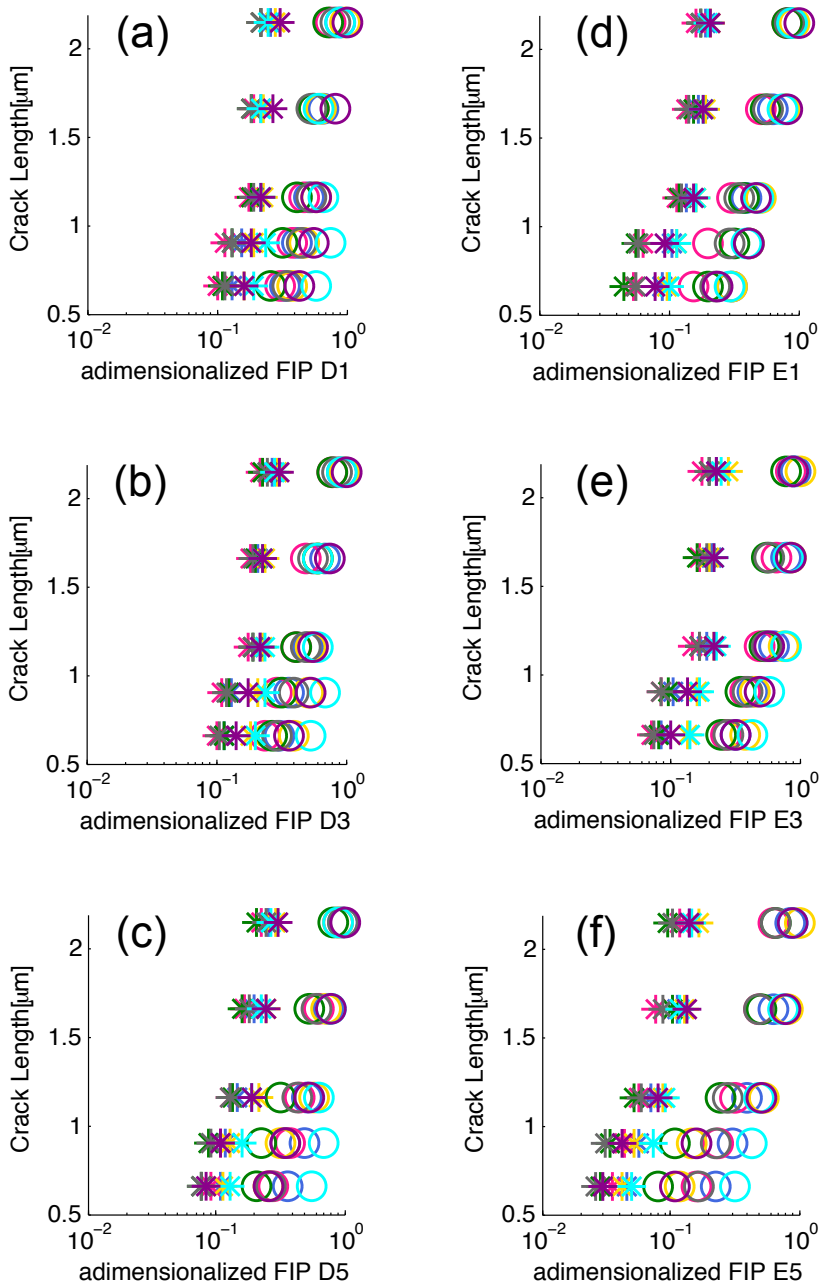


**Figure 4.12:** This figure shows the shape of the nondimensionalized FIPs (w.r.t their maximum) plotted against crack length. The Stars represents a global strain of 0.32% (middle of linear elastic zone), while the open circles represents a strain of 0.56% beginning of elasto-plastic zone.

the variability in short crack behavior as originally constructed by Newman et al. [40] , which depicts the variability in short crack growth rates for a given stress intensity factors. The similarity in shapes of these diagrams is most pronounced in the E5 FIP. This is the second reason why we choose E5 as a suitable reference parameter. Figure 4.13 depicts the possible relation investigated between SCG behavior and the chosen FIP, E5. In Figure 4.13 (a), the

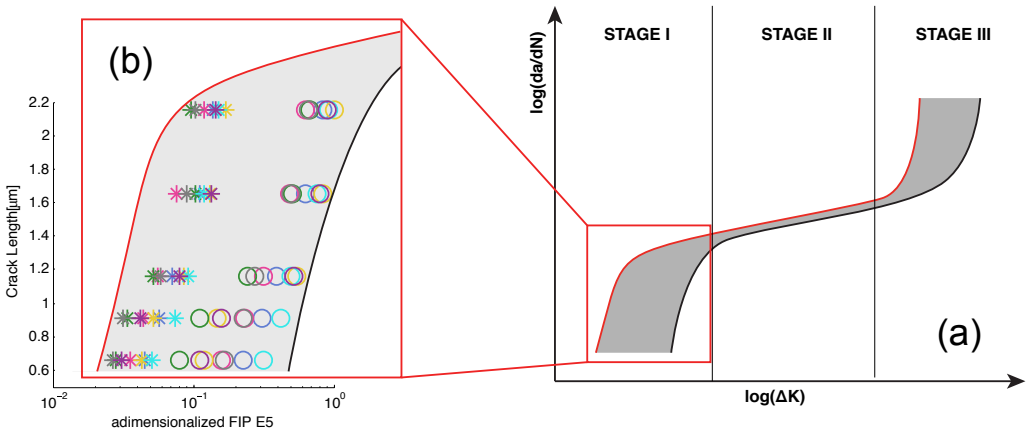


**Figure 4.13:** Analogous behavior between the shape of E5 and small crack behavior. The small crack variability can be related to our quasi static SCG analysis through this indicator parameter that takes into account critical plane dissipated energy as major indicator of damage nucleation and consequent failure.

complete fatigue crack propagation behavior is shown, as well characterized, the variability is more a noticeable in stages 1 and 3 as depicted by the shaded zones.Figure 4.13 (b) displays an enlargement of stage 1, in which we superimpose FIP E5, showing the analogy that we proposed between variability commonly observed in SCG and the reference parameter.

# Chapter 5

# Conclusion

Variability in the microstructure is inherent to engineering alloys, which manifests itself in variability in the short crack growth (SCG) behavior:

- During early stages of crack propagation, the stress fields produced by the crack are small compared with the stress fields produced by the microstructural defects, thus the microstructure plays a crucial role for prediction of fatigue life. This work addresses variability in the microstructure in understanding (non)favorable microstructure features to facilitate SCG.

- Similar orientation can lead to very different behavior ahead of the crack-tip at both macroscopic and microscopic length-scale. Crack propagation is a phenomenon governed by extreme values of resolve shear stress and resolved visco-plastic shear strain reached in proximity of the crack-tip.

- The influence of microstructure variability can be perceived, not only directly ahead of the crack-tip, but also in neighbor grains. Thus, the clusters of grains ahead of the crack tip must be analyzed to determined SCG behavior.

- By successfully addressing microstructure variability, we elucidate the well-known phenomenon of scatter in the crack growth rates in *stage I*

in the conventional Paris' diagram.

From this analysis, there is a critical need to define a microstructure-sensitive definition of the driving force for SCG:

- Microstructure features influence the distribution of the stress fields at the microscopic level, leading to different slip system activation that will in turn influence slip irreversibilities and associated SCG behavior/rate.
- From the analysis of the six different fatigue indicator parameters (FIP) analyzed, we identified E5 as the best candidates for a SCG driving force. The parameter E5 accounts for energy dissipation on the critical plane.
- At low strain levels, the direction of maximum FIP in the specimen is driven by the principal stress axes, due to plasticity developing in the small, confined region ahead of the crack. While at higher strain levels, the FIP has a good alignment with the critical plane of maximum shear stress, displaying damage accumulation based on accumulation of plastic strain on multiple slip systems local grain rotation and energy dissipation.
- Fatigue behavior and SCG path are strongly influenced by the interaction between stress/strain fields induced by the crack and those induced by microstructure features. By viewing the interaction of these stress fields, we can postulate on fracture mechanisms, such as grain shielding and crack bifurcation.

## 5.1 Future Works

From the present work a very complex scenario arises. In order to successfully predict short crack growth behavior, namely rate of growth, and crack propagation direction, and to fully address the relationship between them and microstructure variability further studies are needed:

- investigation of variability microstructure features like grain size, crack position and orientation are needed. These investigation will help to understand which characteristic are essential for lower/higher growth rate and self arrest;

- even if at the microscopic scale slip occurs only slip systems and plasticity is caused from shear stress over them, the investigation of different macroscopic load types like shear and torsion need to be investigated. This will help to understand the relationship between macroscopic load type and its redistribution on slip systems;

- in order to successfully predict material failure on the critical slip plane, threshold value of FIP for crack propagation are needed. In order to find it 3D in-situ microstructure characterization during fatigue experiment are needed

- from a computational point of view different tasks are still required to improve the EVP-FFT framework:

  - to improve computational performance and to have the possibility to simulate large microstructure dataset at extremely-high resolution parallelization of the code is required;

  - input parameter need to be improved, in fact to correctly investigate fatigue, the possibility to use complex load/unload history is required;

- the last bullet point but the most important of them all is to compare results obtained with simulation and experiment iteratively in order to validate the framework obtained from these studies and close the loop between simulation and experiment

# Appendix A

# Videos

## A.1 Video #1

## A.2 Video #2

## A.3 Video #3

## A.4 Video #4

# Bibliography

[1] Farid F. Abraham, Robert Walkup, Huajian Gao, Mark Duchaineau, Tomas Diaz De La Rubia, and Mark Seager. Simulating materials failure by using up to one billion atoms and the world's fastest computer: Work-hardening. *Proceedings of the National Academy of Sciences*, 99(9): 5783–5787, 2002. 10.1073/pnas.062054999.

[2] Wael Abuzaid, Michael D. Sangid, Huseyin Sehitoglu, Jay Carroll, and John Lambros. The role of slip transmission on plastic strain accumulation across grain boundaries. In *IUTAM Symposium on Full-Field Measurements and Identification in Solid Mechanics, July 4, 2011 - July 8, 2011*, volume 4 of *Procedia IUTAM*, pages 169–178. Elsevier, 2012.

[3] AFRL-WPAFB. Small in100, 2004. Air Force Research Laboratory, Wright-Patterson Air Force Base.

[4] A. S. Argon. Mechanics and physics of brittle to ductile transitions in fracture. *Transactions of the ASME. Journal of Engineering Materials and Technology*, 123(1):1–11, 2001.

[5] R. J. Asaro. Crystal plasticity. *Transactions of the ASME. Journal of Applied Mechanics*, 50(4B):921–34, 1983.

[6] V. P. Bennett and D. L. McDowell. Polycrystal orientation distribution effects on microslip in high cycle fatigue. *International Journal of Fatigue*, 25(1):27–39, 2003.

[7] Erik Bitzek and Peter Gumbsch. Mechanisms of dislocation multiplication at crack tips. *Acta Materialia*, 61(4):1394–1403, 2013.

[8] BlueQuartz. Dream3d official website. `http://dream3d.bluequartz.net`.

[9] R. Brenner, R. A. Lebensohn, and O. Castelnau. Elastic anisotropy and yield surface estimates of polycrystals. *International Journal of Solids and Structures*, 46(16):3018–26, 2009.

[10] M. W. Brown and K. J. Miller. A theory for fatigue failure under multiaxial stress-strain conditions. *Proceedings of the Institution of Mechanical Engineers*, 187(65):745–55, 1973.

[11] G. M. Castelluccio and D. L. McDowell. Assessment of small fatigue crack growth driving forces in single crystals with and without slip bands. *International Journal of Fracture*, 176(1):49–64, 2012.

[12] EBSD.com. `http://www.ebsd.com`.

[13] Ali Fatemi and Darrell F. Socie. Critical plane approach to multiaxial fatigue damage including out-of-phase loading. *Fatigue and Fracture of Engineering Materials and Structures*, 11(3):149–165, 1988.

[14] E. Ferrie and M. Sauzay. Influence of local crystallographic orientation on short crack propagation in high cycle fatigue of 316 ln steel. *Journal of Nuclear Materials*, 386-388:666–9, 2009.

[15] Bradley S. Fromm, Kunok Chang, David L. McDowell, Long-Qing Chen, and Hamid Garmestani. Linking phase-field and finite-element modeling for process-structure- property relations of a ni-base superalloy. *Acta Materialia*, 60(17):5984–5999, 2012.

[16] A. George and G. Michot. Dislocation loops at crack tips: nucleation and growth-an experimental study in silicon. In *European Research Confer-*

*ence on Plasticity of Materials - Fundamental Aspects of Dislocation Interactions: Low-Energy Dislocation Structures III, 30 Aug.-4 Sept. 1992*, volume A164 of *Mater. Sci. Eng. A, Struct. Mater., Prop. Microstruct. Process. (Switzerland)*, pages 118–34, 1993.

[17] A. Giannattasio and S. G. Roberts. Strain-rate dependence of the brittle-to-ductile transition temperature in tungsten. *Philosophical Magazine*, 87 (16-17):2589–98, 2007.

[18] Y. Guilhem, S. Basseville, F. Curtit, J. M. Stéphan, and G. Cailletaud. Investigation of the effect of grain clusters on fatigue crack initiation in polycrystals. *International Journal of Fatigue*, 32(11):1748–1763, 2010.

[19] Peter Gumbsch, Joachim Riedle, Alexander Hartmaier, and Hellmut F. Fischmeister. Controlling factors for the brittle-to-ductile transition in tungsten single crystals. *Science*, 282(5392):1293–1295, 1998.

[20] J. D. Hochhalter, D. J. Littlewood, Jr. Christ, R. J., M. G. Veilleux, J. E. Bozek, A. R. Ingraffea, and A. M. Maniatty. A geometric approach to modeling microstructurally small fatigue crack formation: Ii. physically based modeling of microstructure-dependent slip localization and actuation of the crack nucleation mechanism in aa 7075-t651. *Modelling and Simulation in Materials Science and Engineering*, 18(4):045004 (33 pp.), 2010.

[21] G. R. Irwin. Analysis of stresses and strains near end of crack traversing plate. *American Society of Mechanical Engineers – Transactions – Journal of Applied Mechanics*, 24(3):361–364, 1957.

[22] T. Kanit, S. Forest, I. Galliet, V. Mounoury, and D. Jeulin. Determination of the size of the representative volume element for random composites: Statistical and numerical approach. *International Journal of Solids and Structures*, 40(13-14):3647–3679, 2003.

[23] Alexander M. Korsunsky, Daniele Dini, Fionn P. E. Dunne, and Michael J. Walsh. Comparative assessment of dissipated energy and other fatigue criteria. *International Journal of Fatigue*, 29(9-11):1990–1995, 2007.

[24] R. A. Lebensohn, R. Brenner, O. Castelnau, and A. D. Rollett. Orientation image-based micromechanical modelling of subgrain texture evolution in polycrystalline copper. *Acta Materialia*, 56(15):3914–26, 2008.

[25] R. A. Lebensohn, M. Montagnat, P. Mansuy, P. Duval, J. Meysonnier, and A. Philip. Modeling viscoplastic behavior and heterogeneous intracrystalline deformation of columnar ice polycrystals. *Acta Materialia*, 57(5): 1405–15, 2009.

[26] Ricardo A. Lebensohn. N-site modeling of a 3d viscoplastic polycrystal using fast fourier transform. *Acta Materialia*, 49:2723–2737, Aug 2001.

[27] Ricardo A. Lebensohn, Anand K. Kanjarla, and Philip Eisenlohr. An elasto-viscoplastic formulation based on fast fourier transforms for the prediction of micromechanical fields in polycrystalline materials. *International Journal of Plasticity*, 32-33:59–69, May 2012.

[28] S. B. Lee, R. A. Lebensohn, and A. D. Rollett. Modeling the viscoplastic micromechanical response of two-phase materials using fast fourier transforms. *International Journal of Plasticity*, 27(5):707–727, 2011.

[29] Jr. McEvily, A. J. and R. C. Boettner. On fatigue crack propagation in f.c.c. metals. In *International Conference on Mechanisms of Fatigue in Crystalline Solids, 15 Nov. 1962*, volume 11, pages 725–743, 1962.

[30] J.C. Michel, H. Moulinec, and P. Suquet. A computational method based on augmented lagrangian and fast fourier transforms for composites with high contrast. *Computer Modeling in Engineering and Sciences*, 1:79–88, 2000.

[31] J.C. Michel, H. Moulinec, and P. Suquet. A computational scheme for linear and non-linear composites with arbitrary phase contrast. *International Journal of Numerical Methods in Engineering*, 52:139–158, 2001.

[32] G. Michot. Interaction of a dislocation with a crack tip: From stimulated emission to avalanche generation. *Acta Materialia*, 59(10):3864–3871, 2011.

[33] KJ Miller. A historical perspective of the important parameters of metal fatigue and problems for the next century. In *Fatigue*, volume 99, pages 15–40, 1999.

[34] H. Moulinec and P. Suquet. A fast numerical method for computing the linear and nonlinear mechanical properties of composites. *Comptes Rendus de l'Academie des Sciences, Serie II (Mecanique-Physique-Chimie-Astronomie)*, 318(11), 1994.

[35] H. Moulinec and P. Suquet. A numerical method for computing the overall response of nonlinear composites with complex microstructure. *Computer Methods in Applied Mechanics and Engineering*, 157(1-2):69–94, 1998.

[36] H. Moulinec and P. Suquet. Intraphase strain heterogeneity in nonlinear composites: a computational approach. *European Journal of Mechanics, A/Solids*, 22(5):751–70, 2003.

[37] Hael Mughrabi. Cyclic slip irreversibilities and the evolution of fatigue damage. *Metallurgical and Materials Transactions B: Process Metallurgy and Materials Processing Science*, 40(4):431–453, 2009.

[38] A. Navarro and E. R. de los Rios. An alternative model of the blocking of dislocations at grain boundaries. *Philosophical Magazine A (Physics of Condensed Matter, Defects and Mechanical Properties)*, 57(1):37–42, 1988.

[39] P. Neumann. New experiments concerning the slip processes at propagating fatigue cracks. *Acta Metallurgica*, 22(9):1155–65, 1974.

[40] J. C. Newman, E. P. Phillips, and M. H. Swain. Fatigue-life prediction methodology using small-crack theory. *International Journal of Fatigue*, 21(2):109–119, 1999.

[41] paraview.org. `http://www.paraview.org`.

[42] Paul C. Paris, Mario P. Gomez, and William E. Anderson. A rational analytic theory of fatigue. *The trend in engineering*, 13(1):9–14, 1961.

[43] G. P. Potirniche, S. R. Daniewicz, and J. C. Newman. Simulating small crack growth behaviour using crystal plasticity theory and finite element analysis. *Fatigue & Fracture of Engineering Materials & Structures*, 27 (1):59–71, 2004.

[44] James R. Rice and Robb Thomson. Ductile versus brittle behaviour of crystals. *Philosophical Magazine*, 29(1):73–97, 1974.

[45] RO Ritchie and J Lankford. Small fatigue cracks: a statement of the problem and potential solutions. *Materials Science and Engineering*, 84: 11–16, 1986.

[46] Robert O Ritchie and James Lankford. Small fatigue cracks. Technical report, The Metallurgical Society Inc., Warrendale, PA, 1986.

[47] A. D. Rollett, R. A. Lebensohn, M. Groeber, Y. Choi, J. Li, and G. S. Rohrer. Stress hot spots in viscoplastic deformation of polycrystals. *Modelling and Simulation in Materials Science and Engineering*, 18(7), 2010.

[48] Anthony D. Rollett. Texture, microstructure & anisotropy course at carnegie mellon university. `http://neon.mems.cmu.edu/rollett/27750/27750.html`.

[49] J. Rösler et al. *Mechanical behaviour of engineering materials : metals, ceramics, polymers, and composites*. Berlin ; New York, Springer, 2007.

[50] K. Sadananda and G. Glinka. Dislocation processes that affect kinetics of fatigue crack growth. In *Symposium on Defects and Deformation of Crystalline Solids, 2-6 March 2003*, volume 85 of *Philos. Mag. (UK)*, pages 189–203. Taylor & Francis, 2005.

[51] Michael D. Sangid, Tawhid Ezaz, Huseyin Sehitoglu, and Ian M. Robertson. Energy of slip transmission and nucleation at grain boundaries. *Acta Materialia*, 59(1):283–296, 2011.

[52] Michael D. Sangid, Hans J. Maier, and Huseyin Sehitoglu. An energy-based microstructure model to account for fatigue scatter in polycrystals. *Journal of the Mechanics and Physics of Solids*, 59(3):595–609, 2011.

[53] Michael D. Sangid, Garrett J. Pataky, Huseyin Sehitoglu, Richard G. Rateick, Thomas Niendorf, and Hans J. Maier. Superior fatigue crack growth resistance, irreversibility, and fatigue crack growthŰmicrostructure relationship of nanocrystalline alloys. *Acta Materialia*, 59(19):7340–7355, 2011.

[54] C. Scandian, H. Azzouzi, N. Maloufi, G. Michot, and A. George. Dislocation nucleation and multiplication at crack tips in silicon. *Physica Status Solidi (A) Applied Research*, (1):67–82, 1999.

[55] Mahesh Shenoy, Yustianto Tjiptowidjojo, and David McDowell. Microstructure-sensitive modeling of polycrystalline in 100. *International Journal of Plasticity*, 24(10):1694–1730, 2008.

[56] W. F. Smith and J. Hashemi. *Foundations of materials science and engineering*. Boston, Mass., McGraw-Hill, 2010.

[57] Darrel F Socie. Personal communication, 2013.

[58] So Suresh and RO Ritchie. Propagation of short fatigue cracks. *International Materials Reviews*, 29(1):445–475, 1984.

[59] D. Taylor and J. F. Knott. Fatigue crack propagation behaviour of short cracks; the effect of microstructure. *Fatigue & Fracture of Engineering Materials & Structures*, 4(2):147–155, 1981.

[60] C Tome, G.R. Canova, U.F. Kocks, N Christodoulou, and J.J. Jonas. The relation between macroscopic and microscopic strain hardening in f.c.c. polycrystal. *Acta Metallurgia*, 32:1637–1653, April 1984.

[61] M. A. Tschopp and D. L. McDowell. Influence of single crystal orientation on homogeneous dislocation nucleation under uniaxial loading. *Journal of the Mechanics and Physics of Solids*, 56(5):1806–1830, 2008.

[62] vtk.org. file format reference. `http://www.vtk.org/VTK/img/file-formats.pdf`.

[63] A. J. Wilkinson. Modelling the effects of texture on the statistics of stage i fatigue crack growth. *Philosophical Magazine A (Physics of Condensed Matter: Structure, Defects and Mechanical Properties)*, 81(4):841–55, 2001.

[64] G. R. Yoder, L. A. Cooley, and T. W. Crooker. Quantitative analysis of microstructural effects on fatigue crack growth in widmanstatten ti-6al-4v and ti-8al-1mo-1v. *Engineering Fracture Mechanics*, 11(4):805–16, 1979.

[65] Jiaxi Zhang and Somnath Ghosh. Molecular dynamics based study and characterization of deformation mechanisms near a crack in a crystalline material. *Journal of the Mechanics and Physics of Solids*, 61(8):1670–1690, 2013.